

57-39-12

~~CONFIDENTIAL~~

Copy 227  
RM E57G09

NACA RM E57G09

502

001

DL43939

TECH LIBRARY KAFB, NM



# RESEARCH MEMORANDUM

TOTAL-PRESSURE DISTORTION AND RECOVERY OF SUPERSONIC  
NOSE INLET WITH CONICAL CENTERBODY IN  
SUBSONIC ICING CONDITIONS

By Thomas F. Gelder

Classification cancelled (or changed to.....) *Declassified*  
By Authority of: Lewis Flight Propulsion Laboratory

Cleveland, Ohio *NASA c c N Issue #5*

By.....

*1628*

GRADE OF OFFICER MAKING CHANGE)

*15 N 1967*  
DATE

CLASSIFIED DOCUMENT

This material contains information affecting the National Defense of the United States within the meaning of the espionage laws, Title 18, U.S.C., Secs. 793 and 794, the transmission or revelation of which in any manner to an unauthorized person is prohibited by law.

## NATIONAL ADVISORY COMMITTEE FOR AERONAUTICS

WASHINGTON

September 17, 1957

~~CONFIDENTIAL~~

HADC ADJ '57-6769

7026



## NATIONAL ADVISORY COMMITTEE FOR AERONAUTICS

RESEARCH MEMORANDUM

## TOTAL-PRESSURE DISTORTION AND RECOVERY OF SUPERSONIC

## NOSE INLET WITH CONICAL CENTERBODY IN

## SUBSONIC ICING CONDITIONS

By Thomas F. Gelder

## SUMMARY

Ice was formed on a full-scale unheated supersonic nose inlet in the NACA Lewis icing tunnel to determine its effect on compressor-face total-pressure distortion and recovery. Inlet angle of attack was varied from  $0^\circ$  to  $12^\circ$ , free-stream Mach number from 0.17 to 0.28, and compressor-face Mach number from 0.10 to 0.47. Icing-cloud liquid-water content was varied from 0.65 to 1.8 grams per cubic meter at free-stream static air temperatures of  $15^\circ$  and  $0^\circ$  F.

The addition of ice to the inlet components increased total-pressure-distortion levels and decreased recovery values compared with clear-air results, the losses increasing with time in ice. The combination of glaze ice, high corrected weight flow, and high angle of attack yielded the highest levels of distortion and lowest values of recovery. The general character of compressor-face distortion with an iced inlet was the same as that for the clean inlet, the total-pressure gradients being predominantly radial, with circumferential gradients occurring at angle of attack.

At zero angle of attack, free-stream Mach number of 0.27, and a constant corrected weight flow of 150 pounds per second (compressor-face Mach number of 0.43), compressor-face total-pressure-distortion level increased from about 6 percent in clear air to  $12\frac{1}{2}$  percent after  $2\frac{1}{4}$  minutes of heavy glaze icing; concurrently, total-pressure recovery decreased from about 0.98 to 0.945. For the same operating conditions but with the inlet at  $12^\circ$  angle of attack, a change in distortion level occurred from about 9 percent in clear air to 14 percent after  $2\frac{1}{4}$  minutes of icing, with a decrease in recovery from about 0.97 to 0.94.

## INTRODUCTION

Evaluation of the mission capability of a high-speed, high-altitude, all-weather turbojet aircraft requires a determination of its performance in icing conditions. Because the cruising altitudes of such aircraft are generally above those where icing is likely to occur, and because the high rates of climb or descent involved greatly reduce the duration of an icing encounter under these conditions, elimination of icing-protection equipment may appear attractive. However, the takeoff and landing of these aircraft may present an icing problem, as would an occasional low-altitude loiter requirement where longer icing encounters can occur. For the lower-altitude flight associated with takeoff, climb, descent, loiter, and landing, the desirability of an ice-protection system requires knowledge of the aerodynamic penalties caused by iced aircraft components. Of particular interest are the icing of turbojet inlet components such as cowl lips, centerbody, and centerbody support struts and the effect of this icing on engine performance.

Ideally, air flowing through the compressor face of an axial-flow turbojet engine is at uniform total pressure equal to the free-stream value. Practically, however, the total pressure is less than the free-stream value and frequently not uniform. As indicated in reference 1, this nonideal or distorted flow results from such factors as internal flow separation, rapid duct turns, the presence of struts or other obstructions and protuberances, nonuniform compression with inlet at angle of attack, and operation at off-design inlet conditions. Ice formations on engine-inlet components are examples of protuberances that may magnify the distortion problem.

Distorted flow at the engine compressor face adversely affects engine performance in several ways. Flow distortion at the compressor face has at times caused temperature distortions at the turbine sufficient to require a thrust derating in order to avoid local overheating. Typical results (refs. 2 and 3) indicate as much as a 1-percent thrust derating for each 2-percent total-pressure distortion at the compressor face (where distortion is defined as the maximum local total pressure minus the minimum, divided by the average). For all current turbojet engines, flow distortions depress the surge line and thus reduce the region of surge- and stall-free operation. Consequently, maximum corrected engine speed and altitude limit are reduced while acceleration time and minimum safe engine speed are increased (refs. 3 and 4). Engine airflow distortions also increase vibratory stresses in compressor blading. Studies and proposals for reducing or controlling distortion in clear air are reported in reference 5. The effects of flow distortion depend on the characteristic distortion profile (e.g., radial, circumferential, or mixed) as well as on level or magnitude, and different engines are not equally tolerant of the same distortions. Increased duct velocities and compressor blade loadings of future engines may aggravate the distortion problem.

Various distortion patterns were simulated (by use of screens) in the jet-engine studies of references 2 to 4. Although generalizing the level or pattern of total-pressure distribution to be expected in flight was difficult, the patterns were selected to cover a range that might be encountered. The total-pressure-distortion levels obtained were of the order of 15 to 30 percent.

In order to determine the effect that ice formations on a typical supersonic nose inlet might have on the type and magnitude of airflow distortion and the value of pressure recovery at the compressor face of a turbojet engine, the present investigation was conducted in the NACA Lewis icing tunnel. This study provides values of total-pressure distortion and recovery as a function of corrected weight flow resulting from ice formations on a full-scale supersonic nose inlet. Clear-air data were also taken for comparison. Free-stream and compressor-face Mach numbers were varied over a range from 0.17 to 0.28 and 0.10 to 0.47, respectively; inlet angle of attack from  $0^\circ$  to  $12^\circ$ ; and icing-cloud liquid-water content from 0.65 to 1.8 grams per cubic meter. In general, the data herein represent the low-flight-speed, low-altitude operation of a supersonic airplane (takeoff, landing, loitering), the type most likely to present an icing problem for such an airplane.

## SYMBOLS

A	flow area (see fig. 2(c)), sq ft
$d_{med}$	volume-median droplet diameter, microns
g	acceleration due to gravity, 32.2 ft/sec <sup>2</sup>
M	Mach number
P	total pressure
$\Delta P$	local maximum minus local minimum total pressure
R	gas constant, 53.3 ft/ <sup>OR</sup>
$r_1$	radius of inner cowl (see fig. 2(c))
$r_2$	radius of centerbody (see fig. 2(c))
t	static air temperature, <sup>OF</sup>
V	velocity

$\frac{w\sqrt{\theta}}{\delta}$	corrected weight flow, lb/sec
$w_t$	liquid-water content of icing cloud, g/cu m
$\alpha$	inlet angle of attack, deg
$\gamma$	ratio of specific heats, 1.4
$\delta$	ratio of total pressure to NACA standard sea-level static pressure of 2116 lb/sq ft (29.92 in. Hg abs)
$\theta$	ratio of total temperature to NACA standard sea-level static temperature of 519° R

## Subscripts:

CF	simulated compressor-face station, 85 in. (see fig. 2)
i	inlet station, 1.9 in. (see fig. 2)
0	free stream

## Superscript:

-	area average
---	--------------

## APPARATUS

## Model and Installation

A front view of the supersonic-nose-inlet model installed in the 6- by 9-foot test section of the Lewis icing tunnel is shown in figure 1. The over-all length of the installation was about 20 feet, with a main support pedestal located near the midpoint. Additional support was provided by an A-frame just aft of the inlet lips. A prototype (full-scale) inlet was used for the first few feet of the external cowl and the first 7 feet within the inlet model (forward of the compressor-face station). The aft 13 feet of the installation contained the ejector nozzles and ducting used to simulate the pumping action of an engine compressor.

The conical centerbody was supported by three equally spaced swept-back struts mounted from the outer shell or cowl, as indicated by the schematic drawing of the inlet and afterbody in figure 2(a). The over-all top view of figure 2(a) shows the inlet at 12° angle of attack. Because of the model and tunnel size, only the forward half of the installation was at angle of attack relative to the free stream. Transition sections

were inserted between the inlet and afterbody to effect angles of attack of  $4^\circ$ ,  $8^\circ$ , and  $12^\circ$  in a plane parallel to the tunnel floor; thus, the actual nacelle top was rotated  $90^\circ$  from the tunnel top position. This model orientation, which was selected to best utilize the larger dimension of the tunnel test section (9 ft floor width), introduces no unreal effects on flight simulation.

The nacelle stations (inches) marked on figure 2(a) are referenced to a transverse plane 1.9 inches upstream of the inlet lips. The tip of the conical centerbody ( $25^\circ$  half-angle) is  $5\frac{1}{2}$  inches upstream of station 0. The  $1\frac{1}{2}$ -inch air gap shown just aft of the conical tip was used for discharging hot air from the centerbody anti-icing system, which was inoperative for the studies reported herein. The conical centerbody faired in to a cylindrical section at station 20. At the end of the straight cylindrical section (station 35), the centerbody narrows to a smaller cylindrical section that ends at the instrumented compressor-face station 85. A conical tailpiece closes the centerbody contour. Aft of the tailpiece are the transition sections for angle-of-attack simulation. The 19 ejector nozzles are located between stations 120 and 139, and a butterfly valve is at station 211. The afterbody ducting ends at station 240.

The front-view schematic drawing of the inlet shown in figure 2(a) indicates the positions of the three centerbody struts and the sub-inlet as mounted in the tunnel. This sub-inlet, which provides air for oil-cooling, is one of three included in the prototype design. A side view of the sub-inlet (located between stations 35 and 104) is also shown. Airflow through the sub-inlet is independently controlled by two ejector nozzles (one shown) and a butterfly valve. A front-view photograph of the inlet model showing the support struts and sub-inlet is given in figure 2(b).

Figure 2(c) presents the annular flow areas within the main inlet from the cowl-lip station 1.9 to the compressor-face station 85. These flow areas at any nacelle station, which are calculated on the assumption that the airflow across the annulus is parallel to the mean radius at that station, account for the presence of the centerbody support struts. Significant airflow areas are: inlet lips (station 1.9), 4.576 square feet; inlet throat (station 20), 3.40 square feet; and compressor face (station 85), 4.549 square feet. An enlarged schematic drawing of the inlet lips is shown in figure 2(d).

The nineteen ejector nozzles, in the symmetrical array shown in figure 2(a), received primary air by means of a high-pressure service line. This airline was brought through the tunnel floor and into a ring manifold formed by the inner and outer walls of the ejector duct. The airline also served as the main support pedestal for the model. Flow of

high-pressure air through the ejector nozzles was required to achieve inlet velocity ratios greater than 1.0. The butterfly valve (station 211) was used to regulate the airflow for inlet velocity ratios less than 1.0. Although both the ejectors and the butterfly valve for the main inlet are shown in operation for convenience of illustration in figure 2(a), they were used independently.

### Instrumentation

As shown in figure 3, model instrumentation consisted of 16 rakes (electrically heated coaxial pressure tubes) and 16 flush wall static taps, eight on the centerbody and eight on the cowl inner wall. All model instrumentation was at the simulated compressor face (station 85); a photograph looking upstream at this station is shown in figure 3(a). A schematic drawing looking downstream at the compressor-face instrumentation is presented in figure 3(b). The five concentric rings of total-pressure tubes were located in equal annular flow areas. The eight pairs of flush wall static taps were spaced midway between adjacent rakes. In addition, one ring of stream static tubes was located at about the average radius of the flow annulus. The three centerbody support struts, although about 3 feet upstream of the compressor-face station, are dashed in on figure 3(b) for convenient reference.

The compressor-face total pressures were measured by an integrating multitube manometer board, and the static pressures by a conventional multitube manometer board. Readings from these manometers were photographically recorded.

### PROCEDURE

In a typical icing test, free-stream Mach number and temperature and compressor-face Mach number were established in clear air. The desired compressor-face Mach number was obtained by regulating the pressure of the primary air to the ejector nozzles or by the position of the butterfly valve. After recording the clear-air data, the water sprays were turned on and the unheated model was allowed to ice. Free-stream conditions were maintained constant during the icing period, but no adjustments were made to maintain the initial compressor-face Mach number. Pressures at the simulated compressor-face station were recorded at 1- to 2-minute intervals throughout the icing period. After a 5- to 10-minute total icing time, the tunnel and model airflow were stopped and the iced model was photographed.

The test conditions are summarized in the following table:

Angle of attack, $\alpha$ , deg	Free-stream Mach number, $M_0$	Initial compressor-face Mach number, $\bar{M}_{CF}$	Liquid-water content, $w_t$ , g/cu m	Volume-median drop diam., $d_{med}$ , microns <sup>a</sup>	Free-stream static air temperature, $t_0$ , °F	Run
0 and 4	0.24	0.09-0.45	0	0	40	Clear air
0	0.17	0.46	1.0	11	15	7
	.17	.45	1.8	16	15	6
	.25	.10	1.3	16	15	3
	.26	<sup>b</sup> .47	1.3	16	15	2
	.27	<sup>b</sup> .47	1.3	16	15	1
	.27	.46	.65	11	15	4
	<sup>c</sup> .28	<sup>b</sup> .47	.65	11	0	5
4	0.27	0.46	1.3	16	15	14
8	0.27	0.46	1.3	16	15	13
12	0.24	0.11	1.3	16	15	11
	.27	.46	1.3	16	15	9
	.27	<sup>b</sup> .47	1.3	16	15	8
	.27	.34	1.3	16	15	10
	<sup>c</sup> .28	<sup>b</sup> .47	.65	11	0	12

<sup>a</sup>Droplet diameters herein are volume-median values with a Langmuir "D" size distribution (ref. 6).

<sup>b</sup>Max. possible without choking inlet throat (station 20, fig. 2(c)).

<sup>c</sup>Max. possible for model and tunnel used.

Most of the data herein were obtained for the high range of compressor-face Mach numbers, which is just below the Mach number required to choke the inlet throat and thereby simulates operation near rated engine speed. The low range of compressor-face Mach numbers simulates operation near idle engine speed.

#### ANALYSIS AND PRESENTATION OF DATA

The compressor-face pressure data are reduced to the conventional definition of total-pressure recovery by dividing the area-averaged total pressure  $\bar{P}_{CF}$  by the free-stream value  $P_0$ . Since the total-pressure tubes at the compressor face were located in equal annular flow areas,  $\bar{P}_{CF}$  was readily obtained from the integrating manometer system (see APPARATUS). Total-pressure distortion (percent) is usually and herein defined as the difference between the maximum and minimum total pressure measured at the compressor-face station  $\Delta P_{CF}$  divided by the area-



averaged total pressure  $\bar{P}_{CF}$ . The total pressure is generally at a minimum near the cowl wall; thus, distortion values depend on the number of pressure tubes and the proximity of the outboard tubes to the wall. The outboard pressure tubes are located at about 95 percent of the duct radius, as they usually are in studies of this kind. Corrected weight flow  $(w\sqrt{\theta/\delta})_{CF}$  was determined from the area-averaged compressor-face Mach number and the flow area as follows:

$$\begin{aligned} \left(\frac{w\sqrt{\theta}}{\delta}\right)_{CF} &= \sqrt{\frac{\gamma g}{R}} \times \frac{2116}{\sqrt{519}} \times \frac{\bar{M}_{CF}}{\left(1 + \frac{\gamma-1}{2} \bar{M}_{CF}^2\right)^{\frac{\gamma+1}{2(\gamma-1)}}} \times A_{CF} \\ &= 85.4 A_{CF} \frac{\bar{M}_{CF}}{\left(1 + 0.2 \bar{M}_{CF}^2\right)^3}, \text{ lb/sec} \end{aligned}$$

(where  $A_{CF} = 4.549$  sq ft, fig. 2(c)).

The tunnel data from this investigation are presented in two forms. In the first, curves of total-pressure distortion  $(\Delta P_{CF}/\bar{P}_{CF})100$  (percent) and total-pressure recovery  $\bar{P}_{CF}/P_0$  are given as functions of corrected weight flow at the simulated compressor face  $(w\sqrt{\theta/\delta})_{CF}$ . Corrected weight flow is used as the independent parameter because

(1) Flow distortion is primarily a function of corrected weight flow (ref. 5), and

(2) The use of  $w\sqrt{\theta/\delta}$  aids in the interpretation of results in terms of operation at constant corrected engine speed (ref. 7).

In the second form, the type or character of distortion is shown by contour maps of the ratio of local compressor-face to free-stream total pressure  $P_{CF}/P_0$  for selected icing times. In addition, photographs of the inlet taken at the end of the icing period are presented. The contour maps and icing pictures are presented, for convenience, in the same geometric sense as the model was mounted in the tunnel; that is, the actual nacelle top is rotated  $90^\circ$  from flight orientation.

As described under PROCEDURE, the airflow through the inlet during an icing run was not adjusted for decreases in the initial corrected weight flow (initial compressor-face Mach number) caused by the ice formations on the inlet components. Hereafter, this type of operation is referred to as "tunnel mode of operation." This tunnel mode of operation resulted in static pressures at the simulated compressor face up to 0.8 inch of mercury higher at the end of an icing run than the initial values in clear air. Because the total pressures at the

compressor face continually decrease with icing time, the resultant Mach number  $\bar{M}_{CF}$  (and thus the corrected weight flow  $(w\sqrt{\theta/\delta})_{CF}$ ) decreases. For a typical engine, however, the engine controls would maintain (for a particular free-stream condition) a constant corrected engine speed (within limits) resulting in a constant corrected weight flow. This type of operation is referred to herein as "engine mode of operation."

4440  
CK-2  
The effect of mode of operation in evaluating compressor-face airflow distortion and pressure recovery resulting from iced inlet components is illustrated in figure 4. This figure is a schematic representation of typical total-pressure distortion and recovery data as a function of corrected weight flow. The dashed curves for zero icing time (clear air) indicate the usual trends of distortion increases and recovery decreases with increased corrected weight flow (refs. 5 and 7). Similar but more pronounced trends are noted for the dashed curves for 5 minutes in icing (fixed free-stream icing condition). The solid lines connecting the symbols (number beside each data symbol denotes minutes of icing at a fixed free-stream condition) represent data obtained from a typical tunnel mode of operation. For the tunnel mode, corrected weight flow decreases with icing time; concurrently, distortion and recovery continue to increase and decrease, respectively. Generally, a change in the free-stream icing condition will shift the curves of constant icing time for all icing times greater than 0. Also indicated in figure 4 is the inlet-throat (station 20, fig. 2(c)) choking limit (assuming no losses).

With an engine operating at a constant corrected engine speed, the curve for engine mode of operation would be vertical at a particular constant value of corrected weight flow (dotted line, fig. 4). The shaded areas in figure 4 emphasize the range of divergence between the tunnel mode of operation (solid line) and the engine mode of operation (dotted vertical line). Changes in distortion and pressure recovery with icing time are increased by the engine mode of operation as compared with the tunnel mode. By presenting data for total-pressure distortion and recovery in the form of figure 4, interpretation of results is not completely restricted to the tunnel mode of operation, and a reasonable approximation of losses at constant corrected weight flow (engine mode of operation) is possible.

## RESULTS AND DISCUSSION

Total-pressure distortion and recovery as functions of corrected weight flow are presented in figure 5 for all conditions studied herein. Figures 5(a) to (d) depict four different free-stream icing conditions with the inlet model at zero angle of attack. For a particular icing condition, the effects of angle of attack are illustrated in figures 5(e), (g), and (h), for angles of  $12^\circ$ ,  $8^\circ$ , and  $4^\circ$ , respectively. For  $12^\circ$  angle of attack, figure 5(f) presents data for a less severe icing condition than that shown in figure 5(e). The effects of corrected weight flow,

free-stream icing condition, icing time, angle of attack, and mode of operation are obtained from a study of the data in figure 5. These effects are isolated and presented separately in the following discussion.

#### Clear-Air Results

As described under PROCEDURE, clear-air data were taken as the starting point (zero icing time) for all the icing runs reported. In addition, the model was studied in clear air for  $0^\circ$  and  $4^\circ$  angle of attack and free-stream Mach number of 0.24 over a range of corrected weight flows from 35 to 155 pounds per second (figs. 5(a) and (h)). All clear-air data from figure 5 are summarized for convenience in figure 6. From figure 6 at  $0^\circ$  angle of attack and a free-stream Mach number of 0.24, increasing the corrected weight flow from 75 to 150 pounds per second increases total-pressure distortion from 1.2 to 7.1 percent and decreases total-pressure recovery from 0.997 to 0.975. Further increases in corrected weight flow cause the distortion and recovery curves to become asymptotic to a corrected weight flow near 167 pounds per second (the inlet-throat choking limit assuming no losses). Results at  $4^\circ$  angle of attack are nearly the same as those at  $0^\circ$ .

At  $12^\circ$  angle of attack (fig. 6), distortion is increased and recovery decreased compared with similar data at  $0^\circ$  angle. For example, at  $M_0$  of 0.27 and corrected weight flow of 150 pounds per second, distortion and recovery at  $12^\circ$  angle of attack are 9 percent and 0.97, respectively, compared with 5.7 percent and 0.982 for  $0^\circ$  angle of attack.

The clear-air pressure-recovery values at free-stream Mach number of 0.24 and  $0^\circ$  angle of attack (fig. 6) are in agreement with those obtained in reference 8 for a blunt cowl lip at the same conditions. The data of reference 8 also indicate an improvement in clear-air pressure recovery with an increase in free-stream Mach number  $M_0$ . Some substantiation of this improvement is obtained from figure 6 by comparing, at a corrected weight flow of 158 pounds per second and  $0^\circ$  angle of attack, the pressure recovery of 0.974 and about 0.96 at  $M_0$  of 0.27 and 0.17, respectively. This improvement in pressure recovery with increased  $M_0$  is also reflected in a reduced distortion level. Reducing  $M_0$  with constant compressor-face weight flow or Mach number  $\bar{M}_{CF}$  increases the inlet velocity ratio.

As discussed in reference 9 for an inlet in clear air, an inlet velocity ratio less than 1.0 causes the stagnation region to occur inside the cowl lip; hence, the airflow that continues to the compressor face is relatively undisturbed. For inlet velocity ratios greater than 1.0, stagnation occurs on the outer cowl, resulting in possible separation of the flow from the lip in making the turn into the inlet and then to the compressor face. Applying these considerations to the data of figure 6 confirms the trend of greater pressure losses for the lower free-stream Mach number (relatively higher inlet velocity ratio).

4440

Figure 7 shows the effects of corrected weight flow, free-stream Mach number, and angle of attack on the character of distortion in clear air, by means of contour maps of the ratio of local compressor-face to free-stream total pressure  $P_{CF}/P_0$ . These pressure-ratio contours are plotted in 2-percent increments with ratios of 0.98 to 1.00 implied within the area enclosed by the 98-percent contour, and so forth. Values of corrected weight flow, total-pressure distortion, total-pressure recovery, and inlet velocity ratio are tabulated beside each map. The ratio of local static pressure to free-stream total pressure, which is also indicated in figure 7, represents the limiting contour value at the walls.

CK-2 back

For  $0^\circ$  angle of attack (figs. 7(a) and (b)), the total-pressure contours are generally symmetrical with radial gradients. With the higher range of corrected weight flows in figure 7 ( $\approx 155$  lb/sec), the slight pressure valley at the 3 o'clock position results from the presence of an upstream centerbody support strut located in the same plane as one pair of total-pressure rakes (see fig. 3(b)). Total-pressure depressions resulting from the two remaining centerbody support struts (7 and 11 o'clock) are not shown by the data, because the total-pressure rakes were not located directly downstream of these struts (fig. 3(b)), and their pressure reductions consequently were not recorded. An increase in corrected weight flow (fig. 7(a)) or a decrease in free-stream Mach number (fig. 7(b)) increases the pressure gradients, reduces the areas of highest pressure recovery, and results in lower values of average recovery, as previously noted in figure 6.

For  $12^\circ$  angle of attack (fig. 7(c)), the total-pressure contours are symmetrical about their horizontal diameter, the plane in which angle of attack was affected for these studies. For all runs at angle of attack other than  $0^\circ$  there is a pressure valley in a sector about the 9 o'clock position. This valley is most pronounced for the  $12^\circ$  angle data and is caused by the angled oncoming flow. At angle of attack, the oncoming airflow approaches the inlet from the left looking downstream, and hence the 9 o'clock region is the most obstructed by the cowl. Thus, what was a generally symmetrical and radial distortion pattern at  $0^\circ$  angle of attack (figs. 7(a) and (b)) becomes, for  $12^\circ$  angle (fig. 7(c)), a mixed pattern with circumferential gradients due to the angled oncoming flow.

At the higher corrected weight flows and free-stream Mach numbers, the total-pressure asymmetry near the cowl wall between 4 and 5 o'clock positions (figs. 7(b) and (c)) is the result of the mode of sub-inlet operation (see APPARATUS). By inducing positive airflow through the sub-inlet by means of its ejectors, the sub-inlet becomes a local boundary-layer bleed that provides some improvement of compressor-face total pressure in the sub-inlet sector. Some subsequent data will show the result of no sub-inlet ejection, in which case air flows upstream from the sub-inlet into the main inlet (reverse airflow through sub-inlet), resulting in a

decreased total pressure at the compressor face in this sector. Although a quantitative study of the effects of sub-inlet operation is beyond the scope of this investigation, the type of sub-inlet flow is indicated on each clear-air total-pressure-contour map.

### Icing Results

Effect of icing time and intensity at zero angle of attack. - Total-pressure distortion and recovery are plotted as functions of icing time in figure 8 for several icing intensities (several combinations of liquid-water content, droplet diameter, and air temperature). For the tunnel mode of operation (fig. 8(a)), corrected weight flow decreases with increasing icing time as previously discussed. The ratio of corrected to initial corrected weight flow is given for each data symbol (initial value tabulated in key for each run). For the engine mode of operation (fig. 8(b)), corrected weight flow remains constant at the initial value for all icing times.

For both modes of operation total-pressure distortion increases and total-pressure recovery decreases with increasing time in icing, the pressure trends being markedly more severe with the engine mode. (Hereinafter, brackets are used to identify distortion and recovery values obtained from constant-corrected-weight-flow [engine mode] interpretation of the tunnel data.) For example, in figure 8, run 2, distortion increases from about 7 percent in clear air to about 10 percent [16 percent] after  $2\frac{1}{4}$  minutes of icing ( $w_t$  of 1.3 g/cu m,  $d_{med}$  of 16 microns,  $t_0$  of 15° F, and  $M_0$  of 0.26). Concurrently, total-pressure recovery decreases from 0.968 to 0.955 [0.934]. A reduction in icing intensity from 1.3 grams per cubic meter and 16 microns to 0.65 gram per cubic meter and 11 microns (run 4, fig. 8) reduces distortion and improves recovery. After  $2\frac{1}{4}$  minutes of run 4, total-pressure distortion and recovery are about 8 percent [10 percent] and 0.973 [0.967], respectively.

Comparison of run 1 (initial corrected weight flow of 161.5 lb/sec) with run 2 (initial corrected weight flow of 159.2 lb/sec) in figure 8 emphasizes the sensitivity of distortion level and, to a lesser extent, recovery to small changes in the initial corrected weight flow when this value approaches that required to choke the inlet throat (see figs. 5 and 6). The distortion level is higher for run 1 than for run 2 for all icing times; and the difference due to corrected weight flow is greatest in clear air, decreases with time in icing, and remains about constant for icing times greater than 2 minutes. For the range of conditions studied, changing icing-cloud temperature from 15° F (run 4) to 0° F (run 5) had little effect on increasing distortion or reducing recovery with time in icing. The different levels illustrated for runs 4 and 5 in figure 8 result primarily from different initial values of corrected weight flow.

4440

The effect of icing time and intensity on total-pressure distortion and recovery is illustrated also by the photographs and pressure-contour maps of runs 1 and 4 in figures 9(a) and (b), respectively. The ice formed on the inlet components after  $6\frac{1}{2}$  minutes of run 1 ( $w_t$  of 1.3 g/cu m,  $d_{med}$  of 16 microns) is the rough and knobby glaze type, which exhibits its characteristic tendency to grow perpendicularly to the local airflow. Individual lumps of ice are symmetrically located around the conical centerbody forward of its maximum diameter. Mushroom-type ice formations appear on the leading edges of the centerbody support struts. Ice on the cowl lip is nearly symmetrical, the formation inclining inward toward the model centerline. In comparison with run 1 (fig. 9(a)), the ice formed on the inlet after  $6\frac{3}{4}$  minutes of run 4 (fig. 9(b)) is the smooth and streamlined rime type, which tends to grow parallel to the local airflow.

The glaze-ice formations of run 1 are considerably larger than the rime-ice formations of run 4 and cause more disturbances to the inlet airflow, as reflected in the tabulated values of distortion and recovery and in the corresponding total-pressure-contour maps. Except for the local flow disturbances caused by the 3 o'clock support strut and the sub-inlet between the 4 and 5 o'clock positions previously discussed, the total-pressure contours are generally symmetrical, with radial gradients or distortion. At zero icing time the pressure gradients are most severe near the cowl wall. With time in icing the gradients increase near the cowl and centerbody and extend farther into the flow annulus, thereby reducing the area of high pressure recovery. The photographs and pressure-contour maps for glaze-icing run 1 in figure 9(a) are typical of those obtained for the other glaze-icing runs 2 and 6 (figs. 5(a) and (c), respectively). Likewise, figure 9(b) for run 4 is typical for the other rime-icing runs 5 and 7 (figs. 5(b) and (d), respectively).

Effect of inlet velocity ratio at zero angle of attack. - As previously discussed for the clear-air data, the air stagnation region shifts from inside the cowl lip at inlet velocity ratios less than 1.0 to outside the cowl lip at inlet velocity ratios greater than 1.0. The shift in air stagnation likewise shifts the location of cowl-lip ice formations. For example, the icing photographs of figure 10(a) show glaze-ice formations on the inner but not outer cowl lip for run 3 at an inlet velocity ratio of 0.45. At inlet velocity ratio of 2.29 (run 6), the photographs of figure 10(b) show glaze ice on the outer but not the inner cowl lip. Except for run 3, all  $0^\circ$  angle data herein are for inlet velocity ratios greater than 1.0, and hence there are no inner-cowl ice formations. The outer-cowl ice formations alter the effective cowl-lip profile in a manner that tends to lessen the internal flow disturbances incurred with higher inlet velocity ratios, thus reversing the clear-air trends previously discussed. This effect is discussed in the following paragraphs.

Profile sketches of ice on the cowl lip for runs 2, 6, and 5 are presented in figures 11(a), (b), and (c), respectively. The inlet velocity ratios quoted are averages over the icing times shown. The free-stream conditions and values of compressor-face distortion and recovery are tabulated beside each sketch. Because distortion and pressure recovery are primarily functions of corrected weight flow, which varied with icing time in a different manner for each of the runs (see fig. 5), a comparison of inlet velocity ratios based on the tunnel mode of operation is unsuitable. Therefore, the distortion and pressure-recovery values tabulated in figure 11 are for an engine mode of operation (constant corrected weight flow of 157 lb/sec; approximately the initial value for runs 2, 5, and 6) and for an "equivalent" ice catch on the leading-edge region. This equivalent ice catch corrects for the differences in icing time, flight speed, liquid-water content, and collection efficiency of the runs illustrated and thereby normalizes these runs to a common value of leading-edge ice thickness (approx. 0.8 in.).

The sketches of figure 11 reflect the tunnel mode of operation, and they do not depict equivalent ice catches. However, the sketches are considered indicative of the general shape and location for a comparison based on equivalent ice catch and engine mode of operation. The profile sketch of figure 11(a) ( $V_1/V_0 \approx 1.45$ ) shows a glaze-ice formation with a horn protruding forward and into the inlet opening. The glaze formation of figure 11(b) ( $V_1/V_0 \approx 2.38$ ) is pointing away from the inlet entrance in a manner consistent with the higher inlet velocity ratio. The horn protuberance of figure 11(a) results in increased airflow disturbance around the cowl lip and poorer compressor-face flow as compared with figure 11(b). For example, with an equivalent leading-edge ice catch of  $3\frac{1}{2}$  pounds per square foot, distortion and pressure recovery are [20 percent] and [0.915], respectively, for  $V_1/V_0$  of 1.45 compared with [16 percent] and [0.93] for  $V_1/V_0$  of 2.38.

Comparison of a glaze and a rime cowl-lip ice formation at nearly the same inlet velocity ratio is illustrated by figures 11(a) and (c). The smoother rime formation of figure 11(c) results in distortion and pressure-recovery values of [15 percent] and [0.945], respectively, an improvement over the comparable glaze formation values of [20 percent] and [0.915]. Compressor-face distortion and recovery for the rime ice formation (fig. 11(c)) are also an improvement over those obtained at the higher inlet velocity ratio with glaze ice (fig. 11(b)). The distortion and pressure-recovery values also include the effects of ice formations on the centerbody and support struts, while only cowl-lip ice is illustrated by the sketches. However, the contour plots of figure 9 indicate that cowl-lip disturbances are the more controlling factor.

Effect of icing time and intensity at angle of attack. - Total-pressure distortion and recovery are plotted as functions of icing time for  $8^\circ$  and  $12^\circ$  angles of attack in figure 12 in the same manner as previously discussed for  $0^\circ$  angle in figure 8. Run 2 from figure 8 is replotted in figure 12 for convenient reference. In figure 12, total-pressure distortion increases and total-pressure recovery decreases with increasing time in icing for both modes of operation, all angles of attack, and all icing conditions. At  $12^\circ$  angle of attack (fig. 12, run 9), distortion increases from about 11.3 percent in clear air to about 13 percent [17 percent] after  $2\frac{1}{4}$  minutes of glaze icing ( $w_t$  of 1.3 g/cu m,  $d_{med}$  of 16 microns,  $t_0$  of  $15^\circ$  F, and  $M_0$  of 0.27). Concurrently, total-pressure recovery decreases from 0.966 to 0.948 [0.931].

At  $12^\circ$  angle of attack, a reduction in icing intensity from the glaze condition of 1.3 grams per cubic meter, 16 microns, and  $15^\circ$  F (run 9) to a rime condition of 0.65 gram per cubic meter, 11 microns, and  $0^\circ$  F (run 12) reduces distortion and improves recovery. After  $2\frac{1}{4}$  minutes of run 12 (fig. 12) total-pressure distortion and recovery are only slightly less favorable than in clear air.

As shown in figure 13, increasing angle of attack from  $0^\circ$  to  $12^\circ$  increases distortion and reduces recovery in both clear air and in icing (icing duration,  $2\frac{1}{4}$  minutes). These aerodynamic penalties are greater for the iced inlet and for the higher values of corrected weight flow, as previously discussed. In clear air (data from fig. 6) for a corrected weight flow of 150 pounds per second, distortion increases from about 6 to [9] percent and recovery decreases from about 0.98 to [0.97] in going from  $0^\circ$  to  $12^\circ$  angle of attack; but, after a brief glaze-icing encounter ( $2\frac{1}{4}$  min), going from  $0^\circ$  to  $12^\circ$  angle increases distortion from  $12\frac{1}{2}$  to [14] percent and reduces recovery from about 0.945 to [0.94].

Thus a few minutes of glaze icing minimizes angle-of-attack effects on distortion level and recovery.

Photographs of the inlet at  $12^\circ$  angle of attack are shown for glaze and rime icing in figures 14(a) and (b), respectively. Figures 14(c) and (d) illustrate a glaze formation for  $8^\circ$  and  $12^\circ$  angles, respectively, the latter to illustrate the effect of inlet velocity ratio near 1.0. All photographs in figure 14 show an asymmetric ice formation on the inlet due to angle of attack. The ice formation is predominantly on the windward side of the centerbody and cowl; the sheltered surfaces are nearly ice-free. In general, the icing photographs at angle of attack show no ice formations on the inner cowl wall for inlet velocity ratios greater than 1.0, as was also true for  $0^\circ$  angle. The photographs for run 10 (fig. 14(d)) after 5 minutes of glaze icing show traces of ice on the windward inner cowl. The inlet velocity ratio approached 1.0 in this run.



The closeup photographs of run 9 (fig. 14(a)) and run 13 (fig. 14(c)) show a nested cup ice formation on the centerbody which is typical of that on the leading edge of a swept airfoil. Comparison of the two closeup photographs taken after tunnel shutdown in figure 14(c) with that taken after icing spray off but before shutdown shows that about two-thirds of the cowl-lip ice was lost from the nacelle top during shutdown. This 10-minute ice formation blew away from and not into the inlet, the model being at  $8^\circ$  angle of attack with inlet velocity ratio greater than 1.0.

With increasing time in icing, the total-pressure-contour maps of figure 14 maintain the initial clear-air pattern of distortion previously discussed, but the pressure gradients increase and the areas of high recovery are reduced into two annular sectors above and below the horizontal diameter.

Photographs and total-pressure contours for run 14 at  $4^\circ$  angle of attack are not shown, because they were similar to those presented and discussed for  $0^\circ$  angle.

#### Concluding Remarks

Compressor-face total-pressure distortion and recovery are closely related to the particular design and operation of an inlet in clear air or in icing, and the type and location of inlet ice are important factors. Under certain icing and operating conditions the data herein indicate that ice formations on an engine inlet cause increased distortions that may result in significant thrust reductions and surge or stall problems, based on previous data. These penalties to engine performance may be approximated from the data presented herein for an engine with known distortion tolerance.

Although there was little breakoff of ice from the inlet components during these studies, the danger of ice breakoff and ingestion by the engine exists and should be considered with reference to elimination of an inlet icing-protection system. Thus, the possible penalties regarding engine performance and engine damage accruing from inlet icing are such as to favor icing protection for the inlet unless the particular configuration or flight plan reduces the risks of no protection to an acceptable level.

#### SUMMARY OF RESULTS

The effects on compressor-face total-pressure distortion and recovery of ice formations on the unheated supersonic nose inlet studied are summarized as follows:

1. The addition of ice to the inlet components resulted in increased distortion levels and reduced pressure recovery compared with clear-air values, the losses increasing with time in icing.

2. The compressor-face flow losses were greatest for the higher corrected weight flows and angles of attack and for glaze-ice formations. After a few minutes of glaze icing the effects of angle of attack on distortion level and recovery are minimized.

3. The general character of compressor-face distortion with an iced inlet was the same as that for the clean inlet except for steeper pressure gradients (distortion patterns). The pressure gradients with the inlet studied were predominantly radial, with circumferential gradients occurring at angle of attack.

4. From a constant-corrected-weight-flow (150 lb/sec, compressor-face Mach number of 0.43) interpretation of the tunnel data, total-pressure distortion increased from about 6 percent in clear air to 12 $\frac{1}{2}$  percent after 2 $\frac{1}{4}$  minutes of heavy glaze icing. Concurrently, total-pressure recovery decreased from about 0.98 to 0.945. These results are for the inlet studied at 0° angle of attack, a free-stream Mach number of 0.27, a liquid-water content of 1.3 grams per cubic meter, a droplet diameter of 16 microns, and a free-stream static air temperature of 15° F. For comparable operating conditions but with the inlet at 12° angle of attack, a change in distortion level occurred from about 9 percent in clear air to 14 percent after 2 $\frac{1}{4}$  minutes of icing, with a decrease in pressure recovery from about 0.97 to 0.94.

Lewis Flight Propulsion Laboratory  
National Advisory Committee for Aeronautics  
Cleveland, Ohio, July 11, 1957

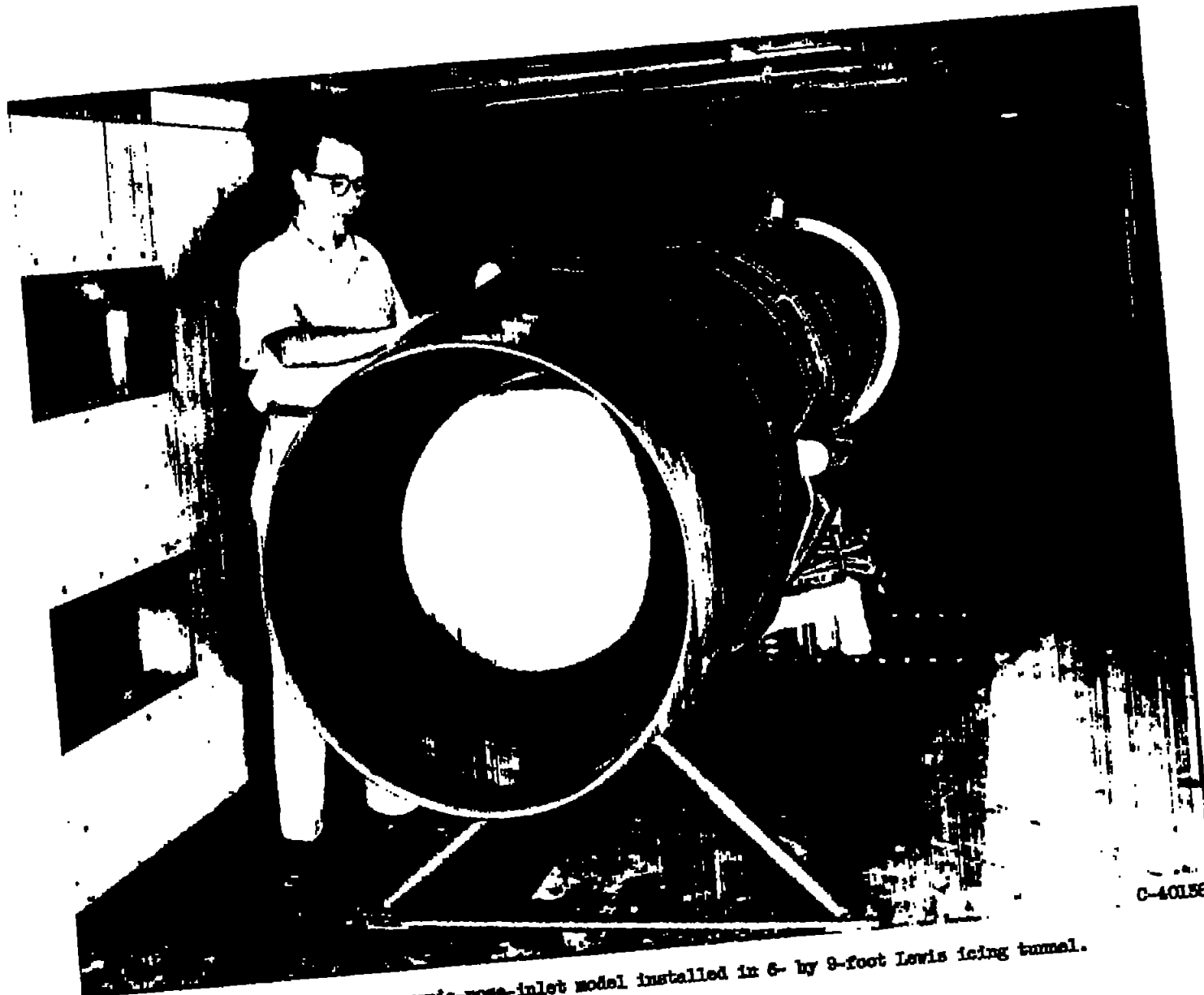
#### REFERENCES

1. Piercy, Thomas G.: Factors Affecting Flow Distortions Produced by Supersonic Inlets. NACA RM E55L19, 1956..
2. Huntley, S. C., Sivo, Joseph N., and Walker, Curtis L.: Effect of Circumferential Total-Pressure Gradients Typical of Single-Inlet Duct Installations on Performance of an Axial-Flow Turbojet Engine. NACA RM E54K26a, 1955.
3. Conrad, E. William, Hanson, Morgan P., and McAulay, John E.: Effects of Inlet-Air-Flow Distortion on Steady-State Altitude Performance of an Axial-Flow Turbojet Engine. NACA RM E55A04, 1955.

4. Smith, Ivan D., Braithwaite, W. M., and Calvert, Howard F.: Effect of Inlet-Air-Flow Distortions on Steady-State Performance of J65-B-3 Turbojet Engine. NACA RM E55I09, 1956.
5. Sterbentz, William H.: Factors Controlling Air-Inlet Flow Distortions. NACA RM E56A30, 1956.
6. Gelder, Thomas F., Smyers, William H., Jr., and von Glahn, Uwe: Experimental Droplet Impingement on Several Two-Dimensional Airfoils with Thickness Ratios of 6 to 16 Percent. NACA TN 3839, 1956.
7. Wyatt, DeMarquis D.: An Analysis of Turbojet-Engine-Inlet Matching. NACA TN 3012, 1953.
8. Blackaby, James R., and Watson, Earl C.: An Experimental Investigation at Low Speeds of the Effects of Lip Shape on the Drag and Pressure Recovery of a Nose Inlet in a Body of Revolution. NACA TN 3170, 1954.
9. Fradenburgh, Evan A., and Wyatt, DeMarquis D.: Theoretical Performance Characteristics of Sharp-Lip Inlets at Subsonic Speeds. NACA Rep. 1293, 1954. (Supersedes NACA TN 3004.)

NACA RM E57G09

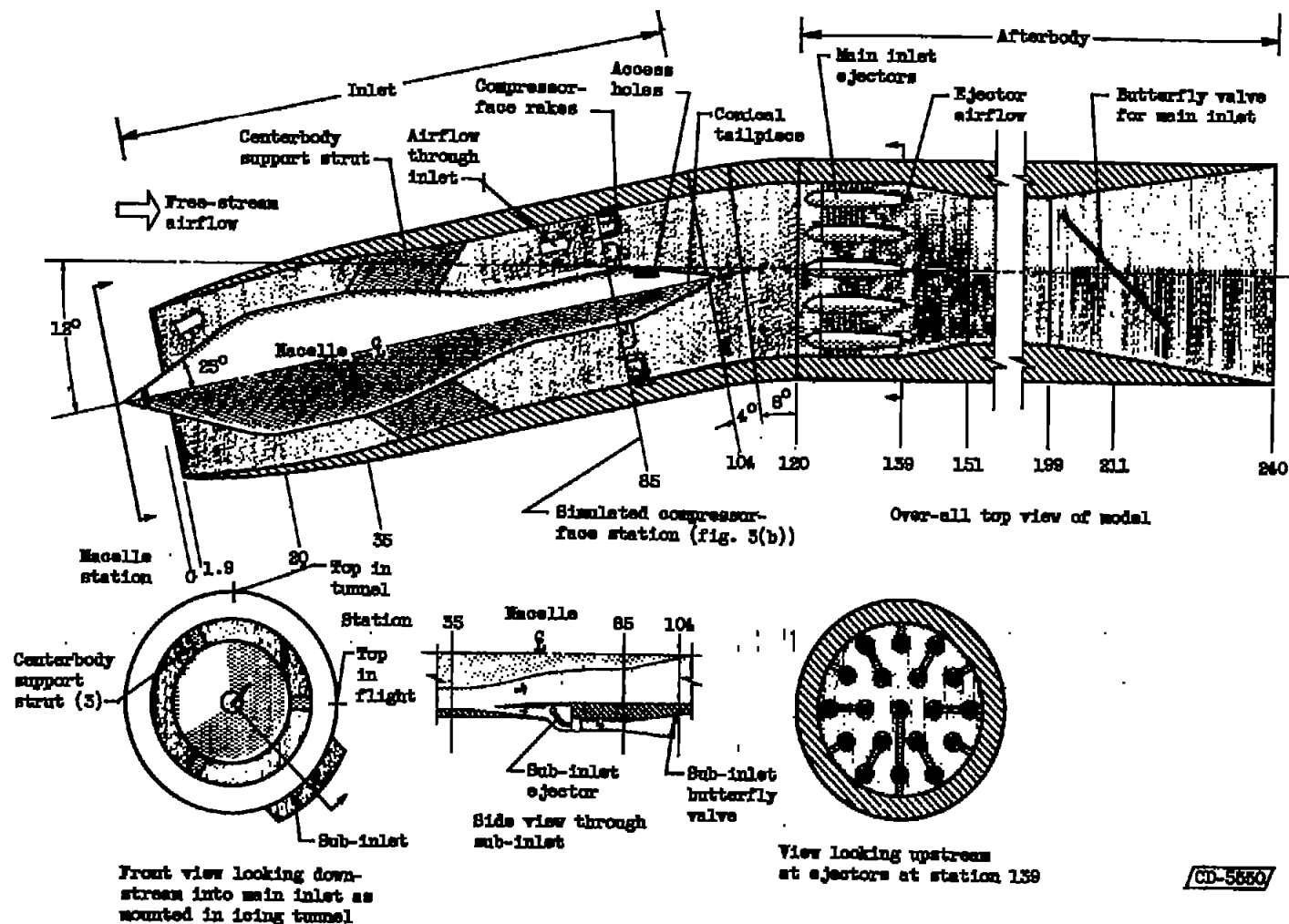
CONFIDENTIAL



C-40158

Figure 1. - Supersonic-nose-inlet model installed in 6- by 8-foot Lewis icing tunnel.

CONFIDENTIAL

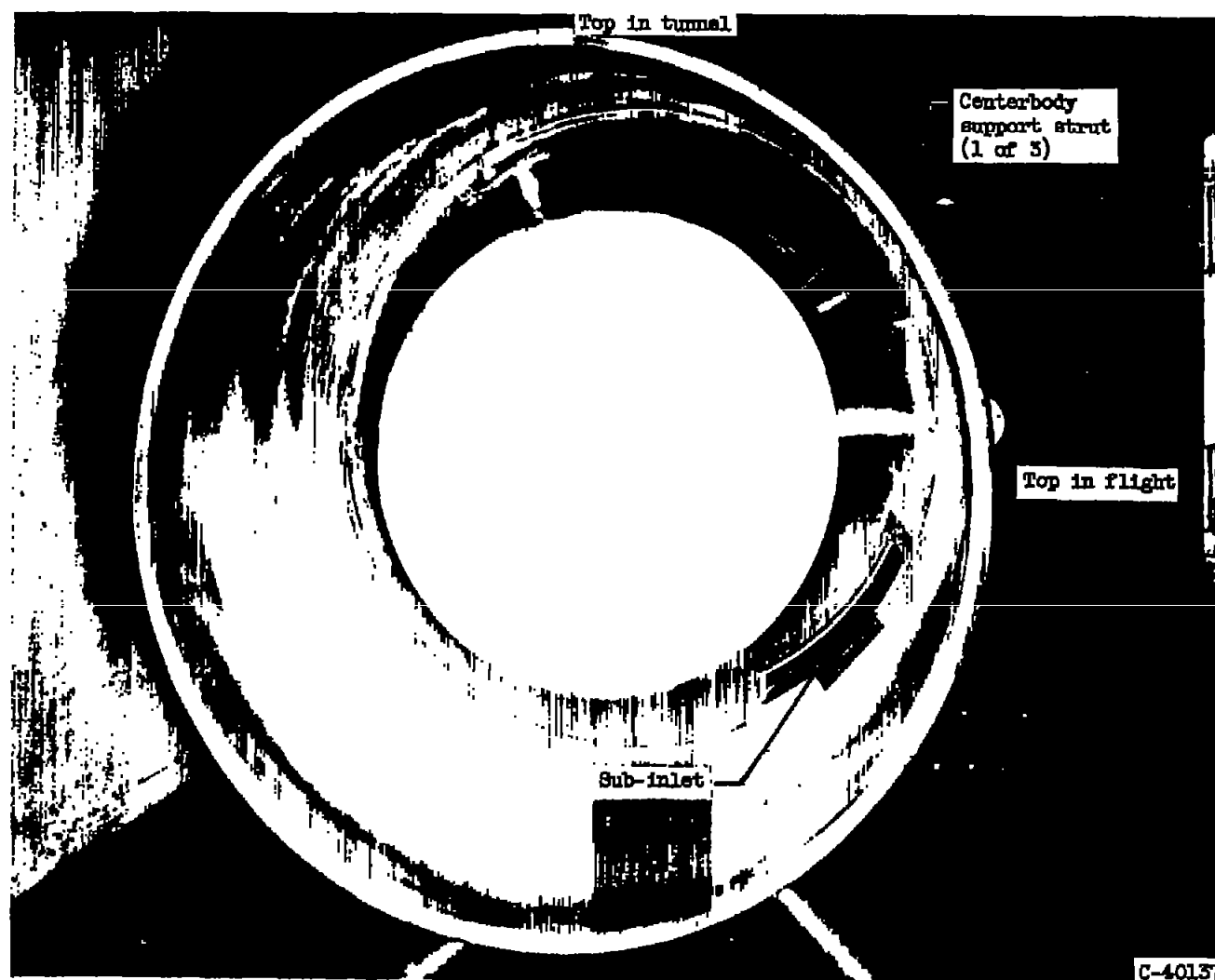


(a) Over-all schematic drawing of inlet and afterbody (inlet at  $12^\circ$  angle of attack).

Figure 2. - Geometry of supersonic-nose-inlet model.

NACA RM E57G08

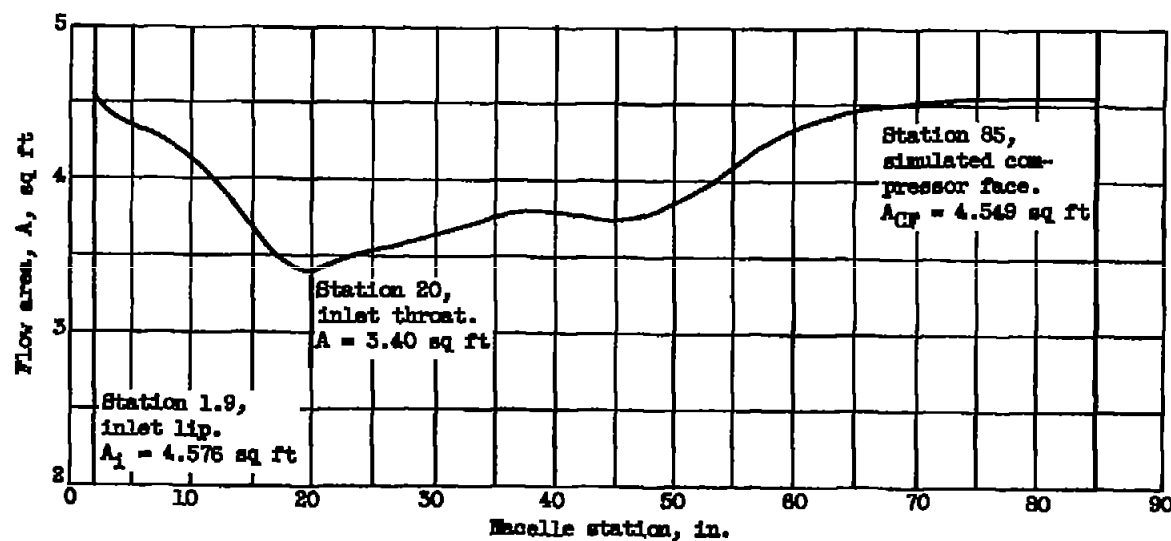
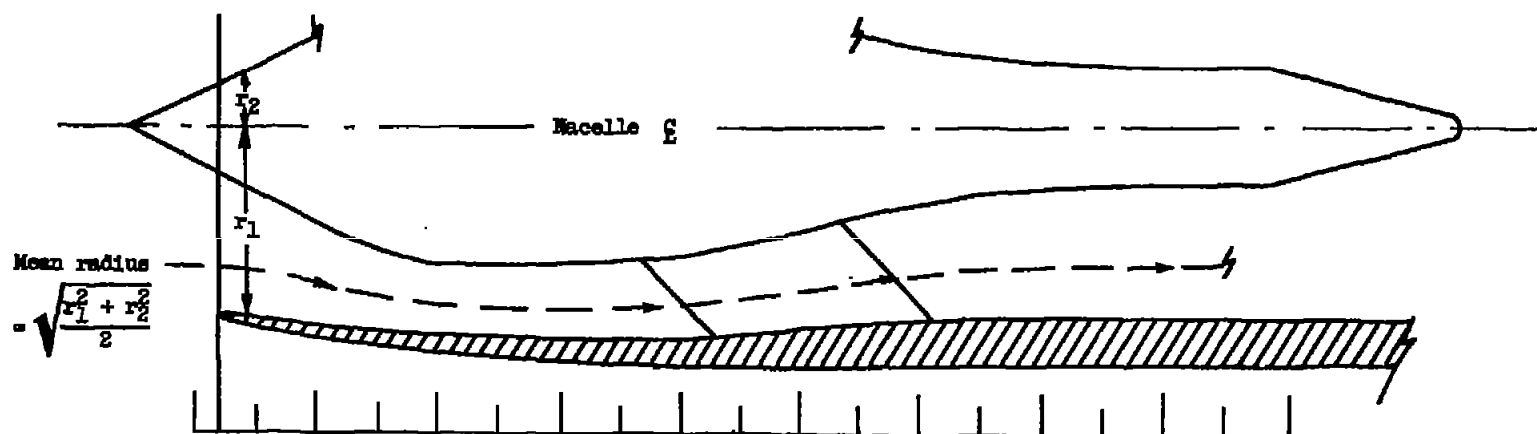
CONFIDENTIAL



(b) Front view of model in tunnel.

Figure 2. - Continued. Geometry of supersonic-nose-inlet model.

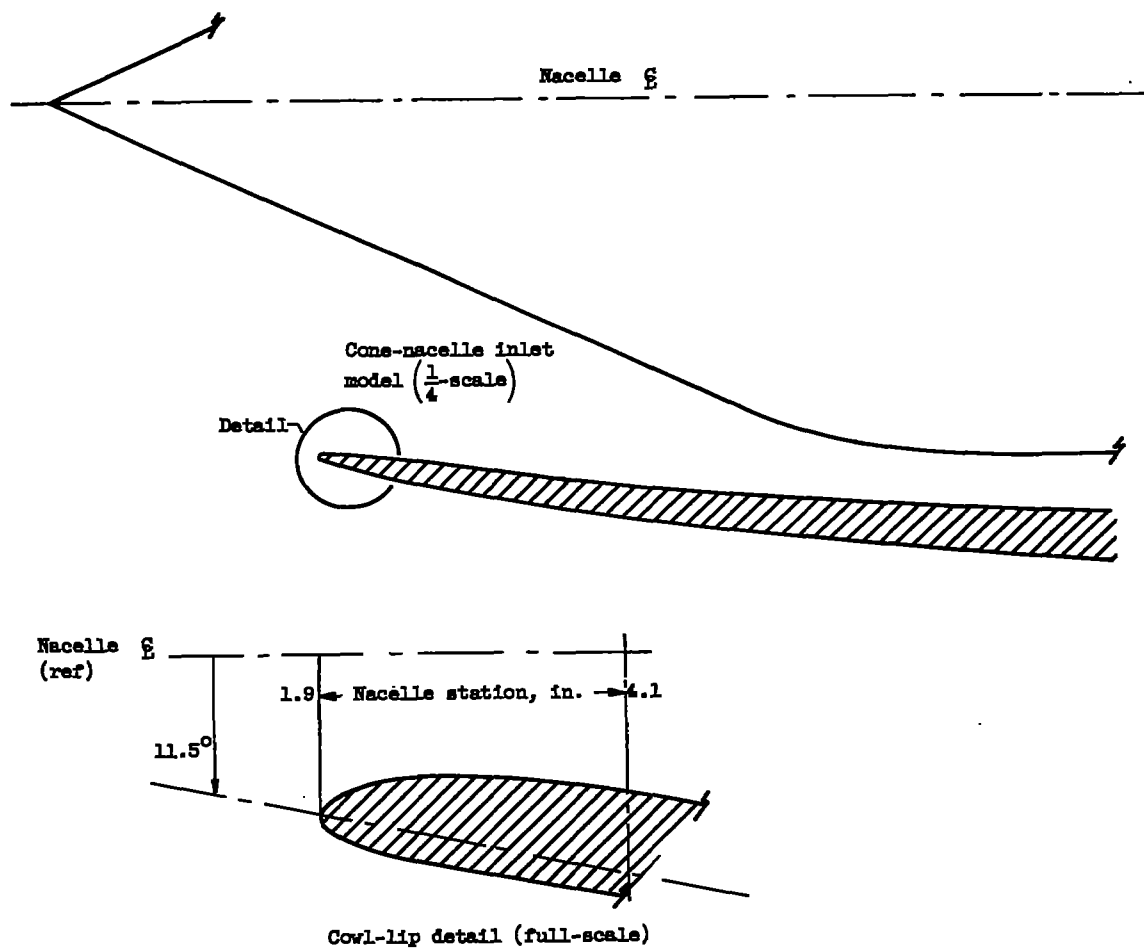
CONFIDENTIAL



(c) Airflow areas within inlet.

Figure 2. - Continued. Geometry of supersonic-nose-inlet model.

CONFIDENTIAL



(d) Schematic drawing of centerbody and cowl-lip detail.

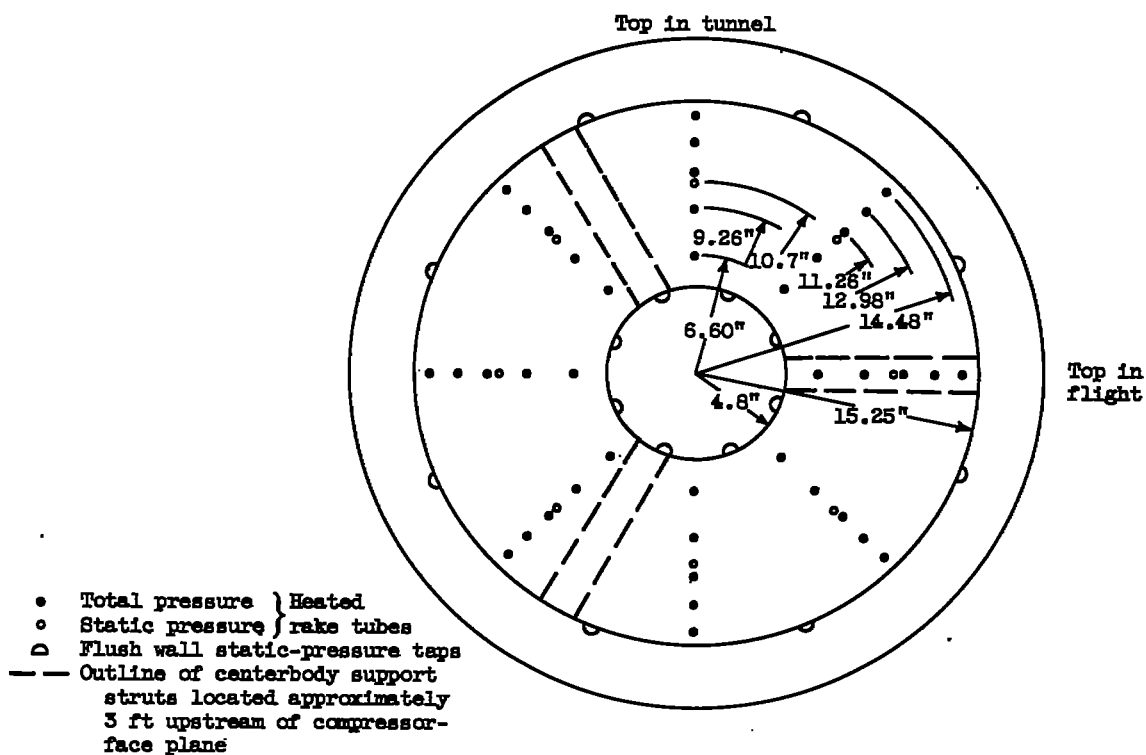
Figure 2. - Concluded. Geometry of supersonic-nose-inlet model.





(a) Photograph looking upstream at compressor face showing electrically heated rakes.

Figure 3. - Pressure instrumentation at compressor-face station of inlet model.



(b) Schematic cross section looking downstream at nacelle station 85 (compressor face) showing location of pressure tubes and taps.

Figure 3. - Concluded. Pressure instrumentation at compressor-face station of inlet model.

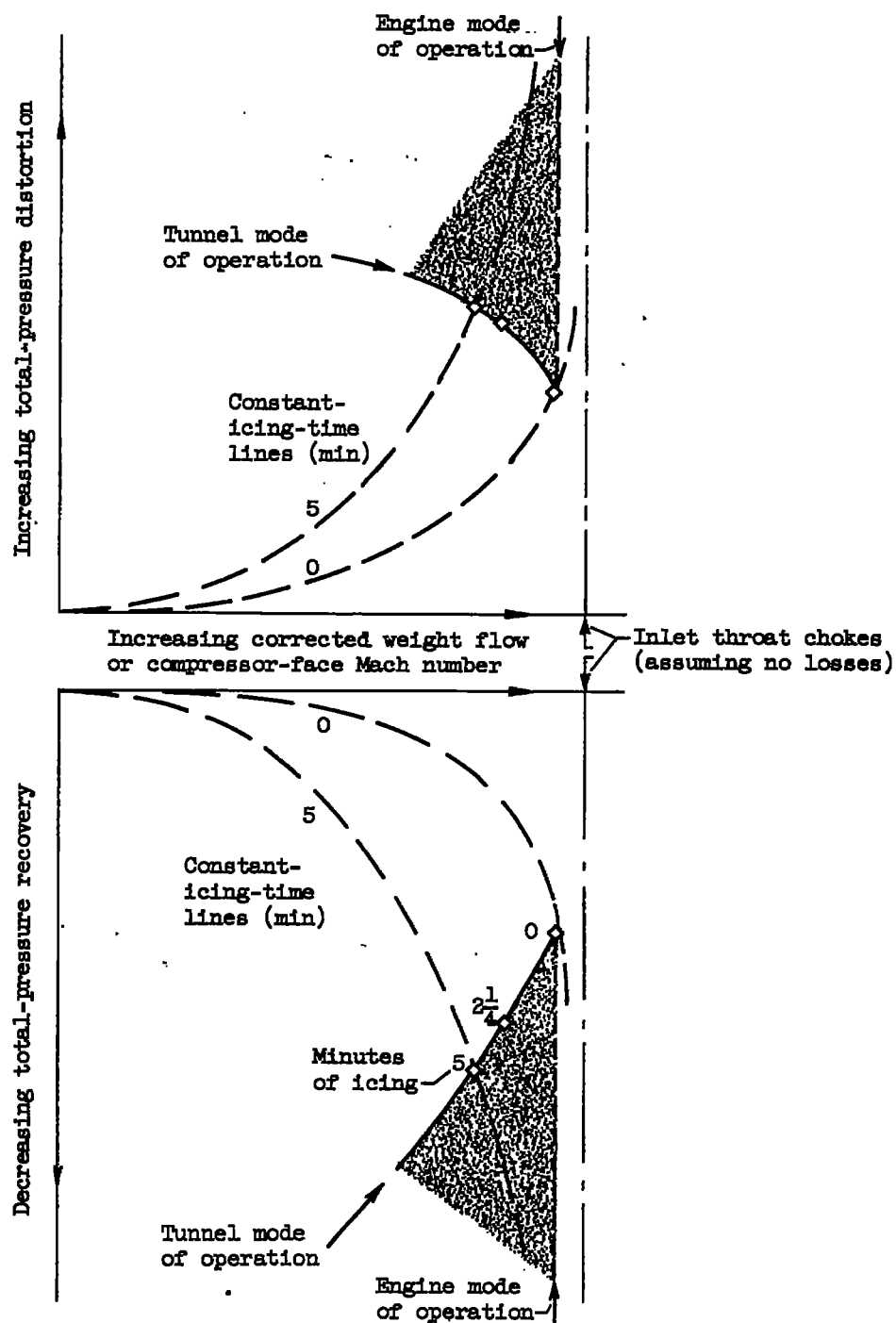


Figure 4. - Schematic drawing showing typical presentation of total-pressure distortion and recovery at diffuser exit (compressor face) of a supersonic nose inlet in subsonic flight and the effect of icing and mode of operation.

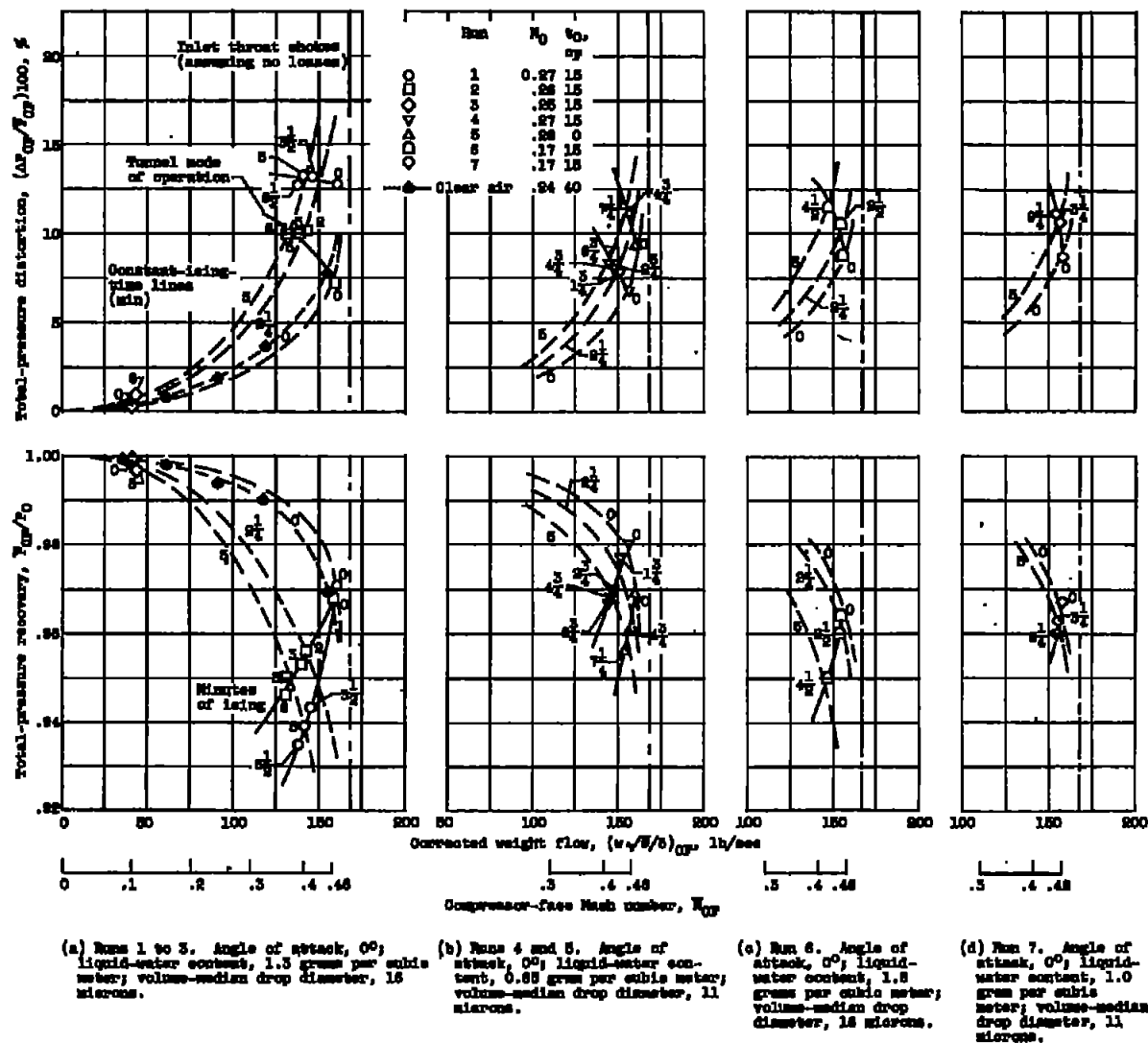


Figure 5. - Total-pressure distortion and recovery at diffuser exit (compressor face) of a supersonic nose inlet in subsonic icing conditions.

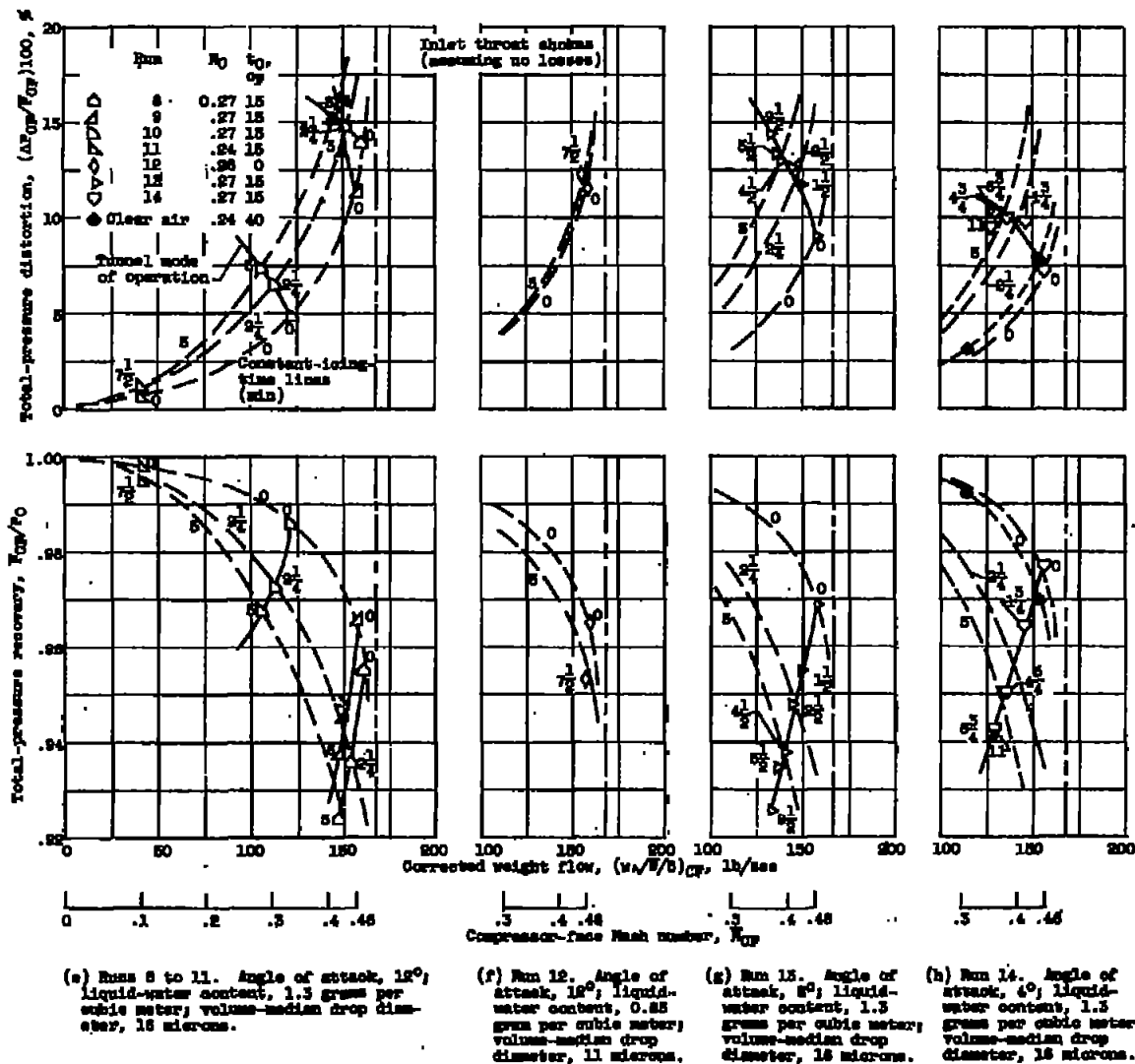


Figure 5. - Concluded. Total-pressure distortion and recovery at diffuser exit (compressor face) of a supersonic nozzle inlet in subsonic icing conditions.

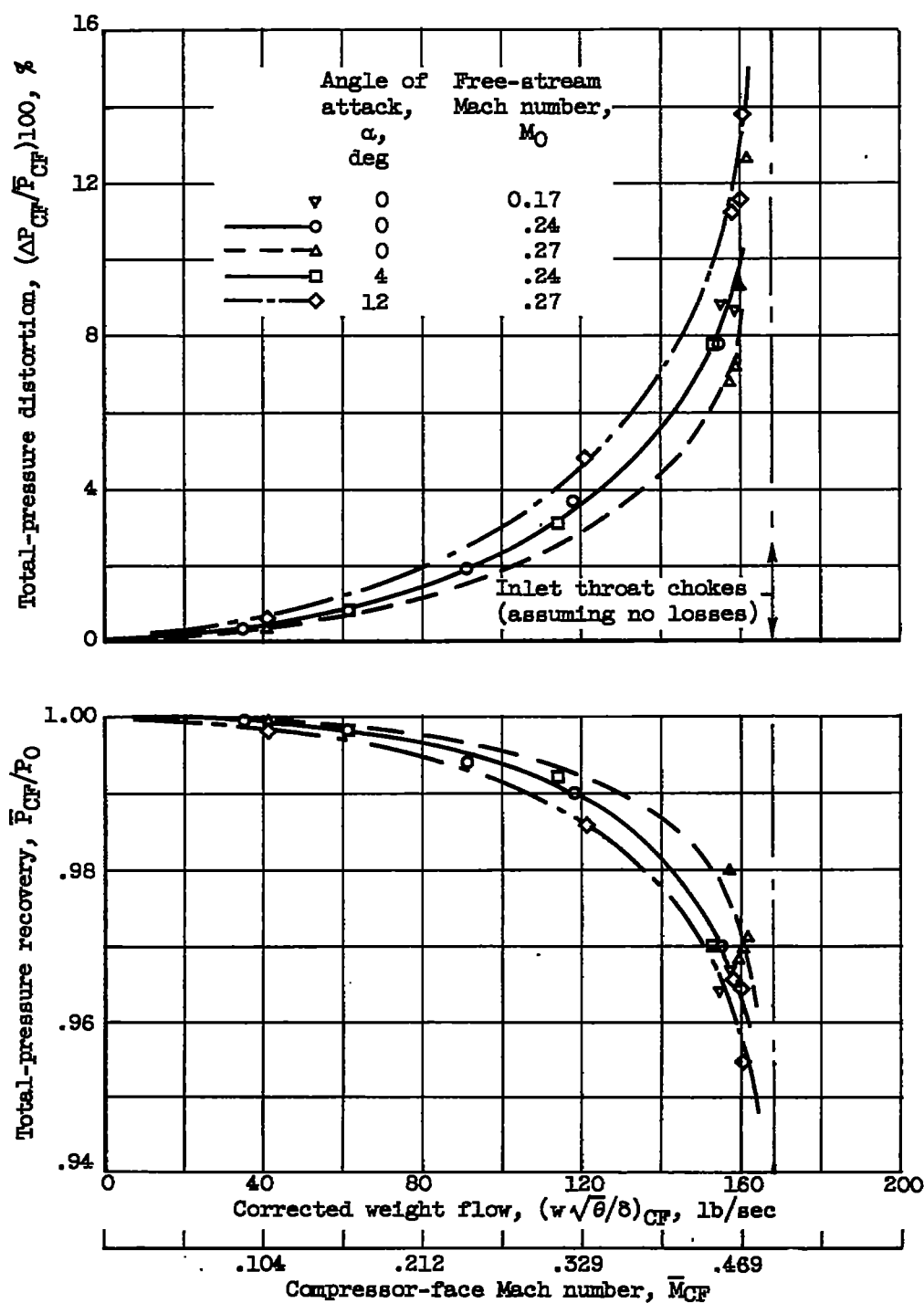


Figure 6. - Total-pressure distortion and recovery at diffuser exit (compressor face) of supersonic nose inlet in subsonic clear air.

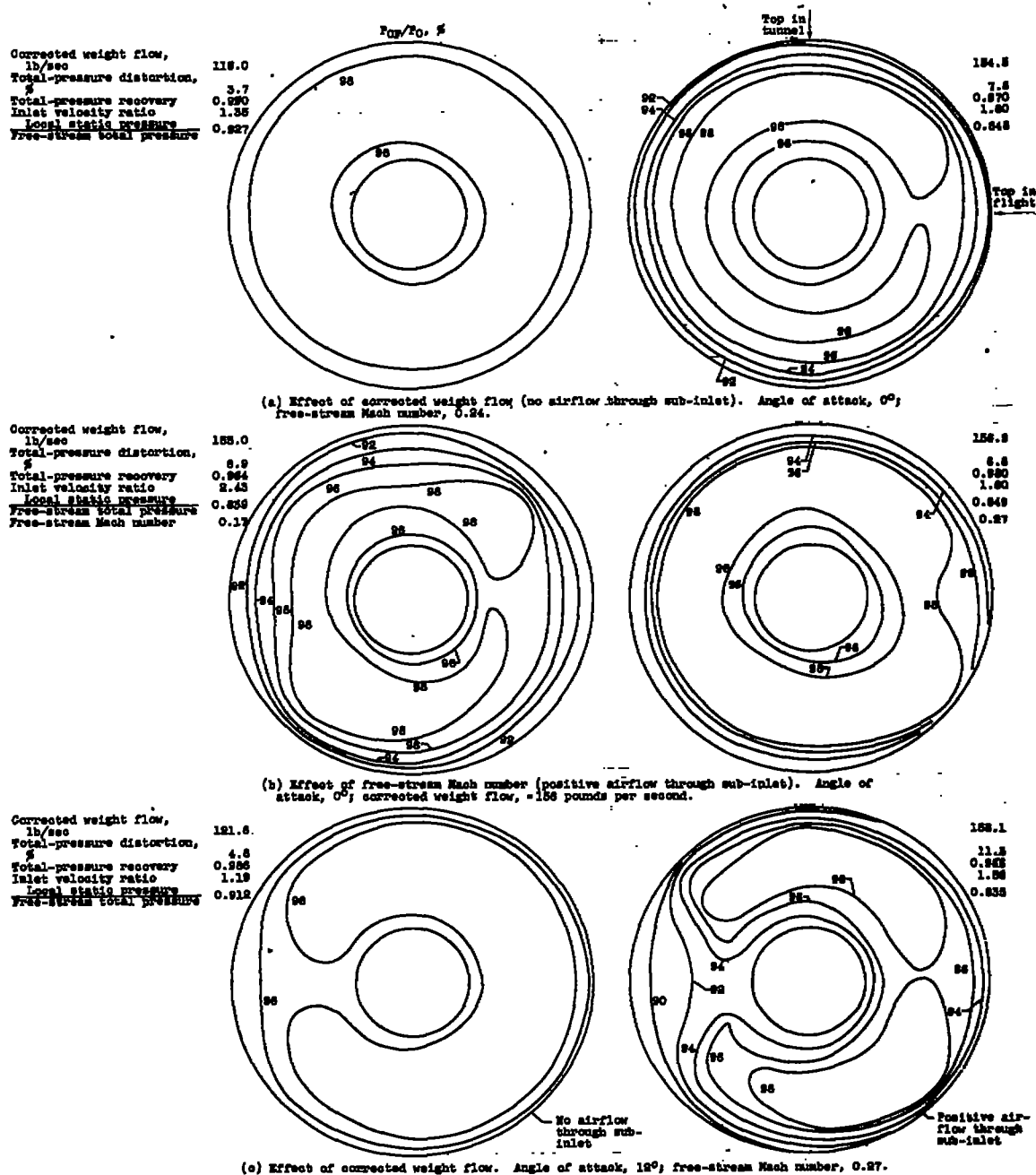


Figure 7. - Effect of corrected weight flow, free-stream Mach number, and angle of attack on maps of ratio of local to free-stream total pressure at compressor face of supersonic nose inlet in subsonic clear air.

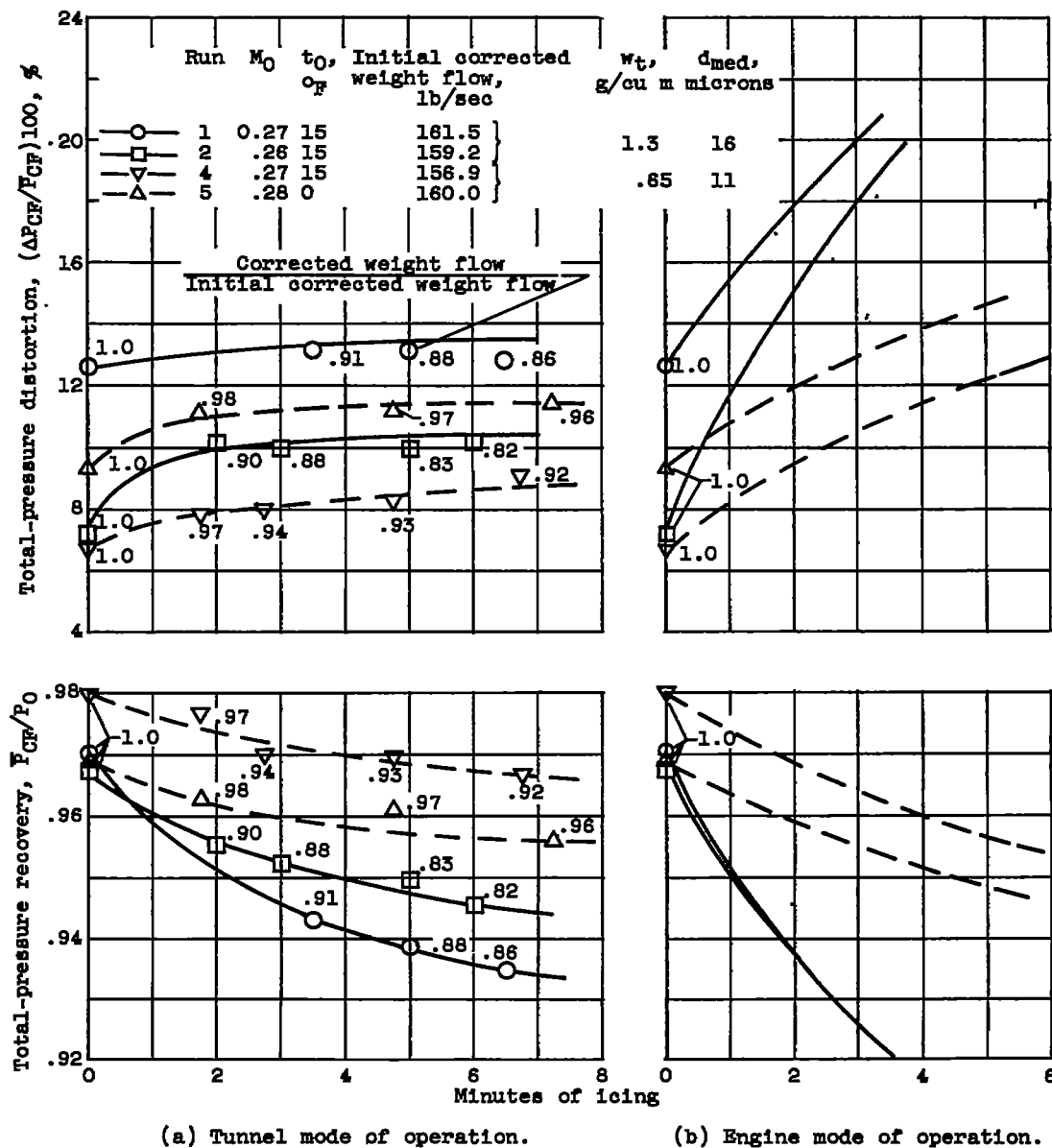
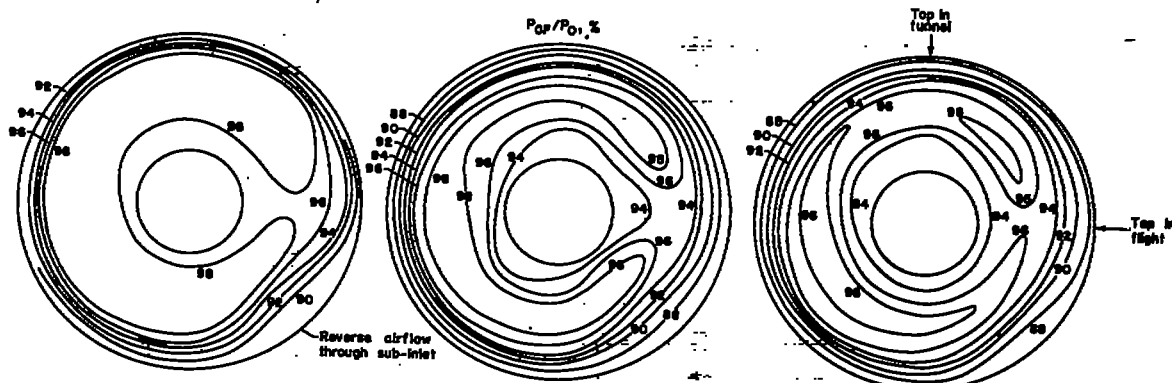
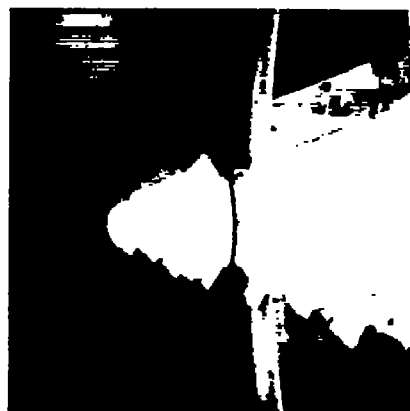


Figure 8. - Effect of icing time and intensity on total-pressure distortion and recovery at diffuser exit (compressor face) of supersonic nose inlet at  $0^\circ$  angle of attack.





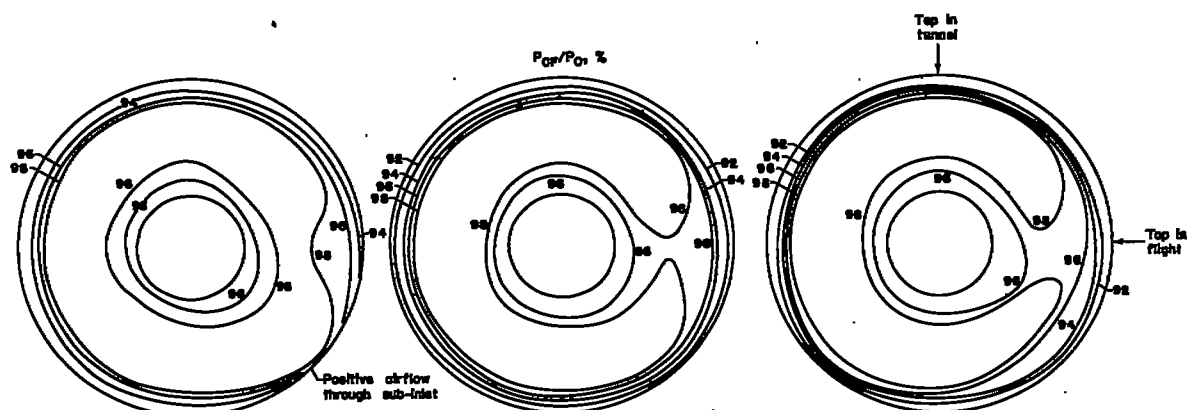
Time in icing, min	0	$\frac{1}{2}$	$6\frac{1}{2}$
Corrected weight flow, lb/sec	161.5	146.4	138.3
Total-pressure distortion, %	12.7	13.2	12.8
Total-pressure recovery	0.971	0.943	0.835
Inlet velocity ratio	1.63	1.43	1.35
Local static pressure	0.832	0.837	0.842
Free-stream total pressure			



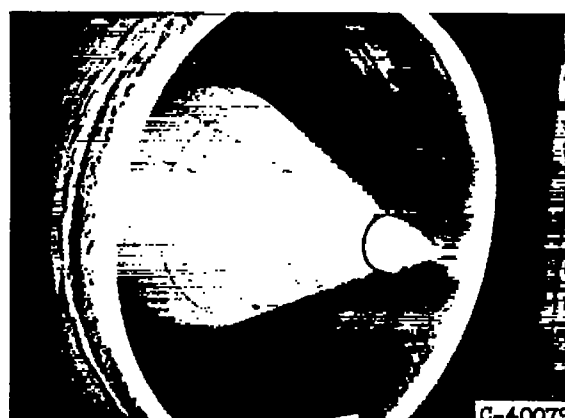
Photographs after  $6\frac{1}{2}$  minutes of icing

(a) Run 1. Free-stream Mach number, 0.27; free-stream static air temperature,  $15^{\circ}\text{F}$ ; liquid-water content, 1.3 grams per cubic meter; volume-median drop diameter, 16 microns.

Figure 9. - Maps of local to free-stream total-pressure ratio at compressor face and photographs of iced model. Angle of attack,  $0^{\circ}$ .



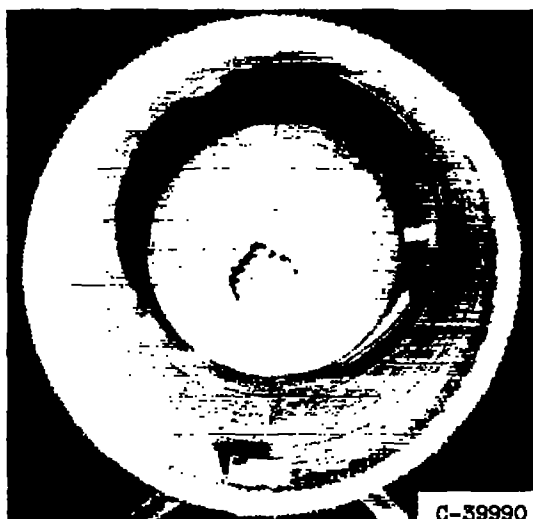
Time in icing, min	0	$2\frac{3}{4}$	$6\frac{3}{4}$
Corrected weight flow, lb/sec	156.9	147.6	144.9
Total-pressure distortion, %	6.8	8.0	9.1
Total-pressure recovery	0.980	0.970	0.967
Inlet velocity ratio	1.60	1.49	1.44
Local static pressure			
Free-stream total pressure	0.849	0.858	0.860



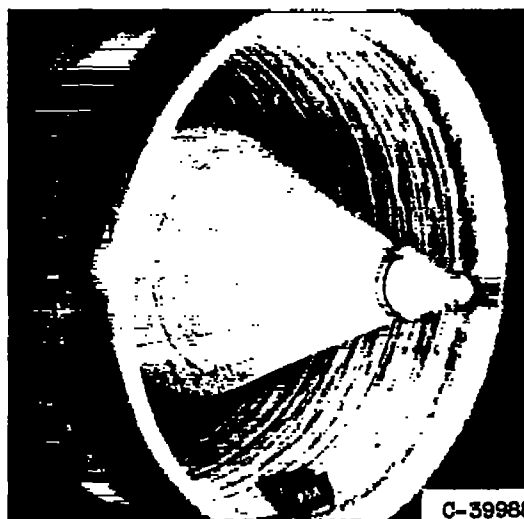
Photographs after  $6\frac{3}{4}$  minutes of icing

(b) Run 4. Free-stream Mach number, 0.27; free-stream static air temperature,  $15^{\circ}\text{F}$ ; liquid-water content, 0.65 gram per cubic meter; volume-median drop diameter, 11 microns.

Figure 9. - Concluded. Maps of local to free-stream total-pressure ratio at compressor face and photographs of iced model. Angle of attack,  $0^{\circ}$ .



C-39990



C-39988

(a) Photographs after 8 minutes of icing, run 3. Inlet velocity ratio, 0.45. Free-stream Mach number, 0.25; liquid-water content, 1.5 grams per cubic meter; corrected weight flow, 43.5 pounds per second; total-pressure distortion, 0.9 percent; total-pressure recovery, 0.997.



C-39887



C-41335

(b) Photographs after  $4\frac{1}{2}$  minutes of icing, run 6. Inlet velocity ratio, 2.29. Free-stream Mach number, 0.17; liquid-water content, 1.8 grams per cubic meter; corrected weight flow, 146.9 pounds per second; total-pressure distortion, 11.5 percent; total-pressure recovery, 0.950.

Figure 10. - Effect of inlet velocity ratio on model ice formations. Angle of attack,  $0^\circ$ ; free-stream static air temperature,  $15^\circ\text{F}$ ; volume-median diameter, 16 microns.

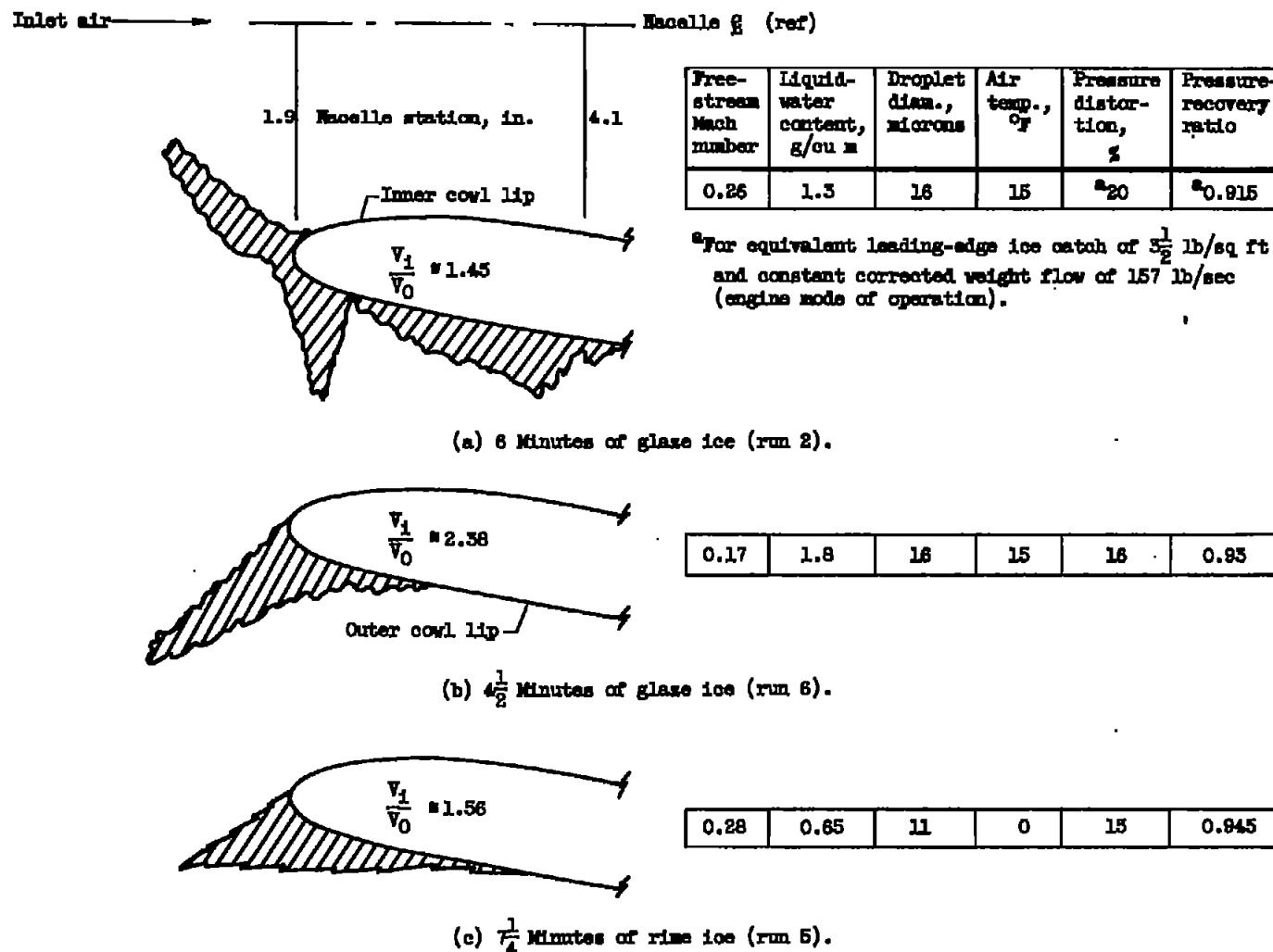


Figure 11. - Effect of inlet velocity ratio on cowl-lip ice formations and on compressor-face total-pressure distortion and recovery of supersonic nose inlet in subsonic icing conditions. Angle of attack, 0°.



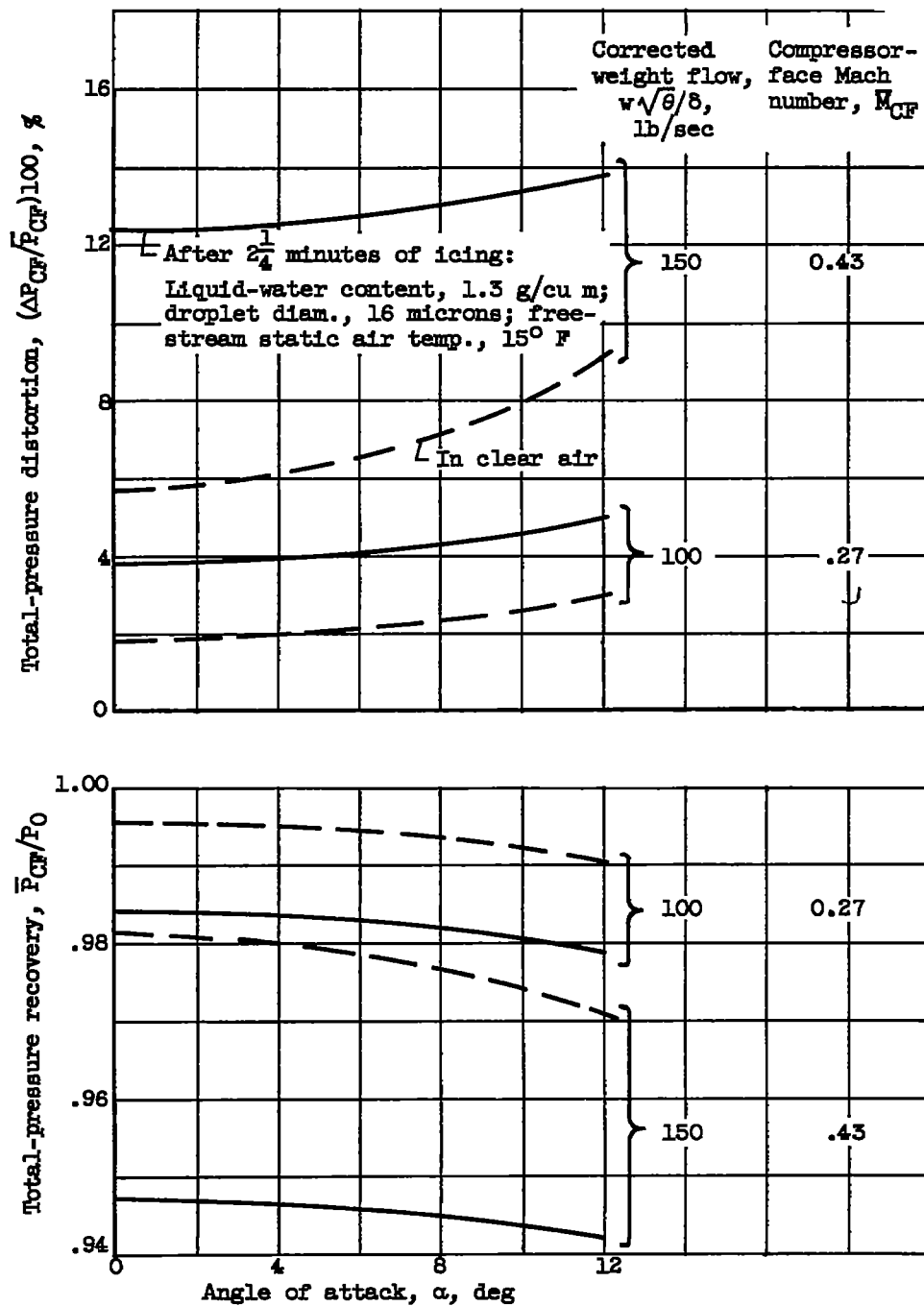
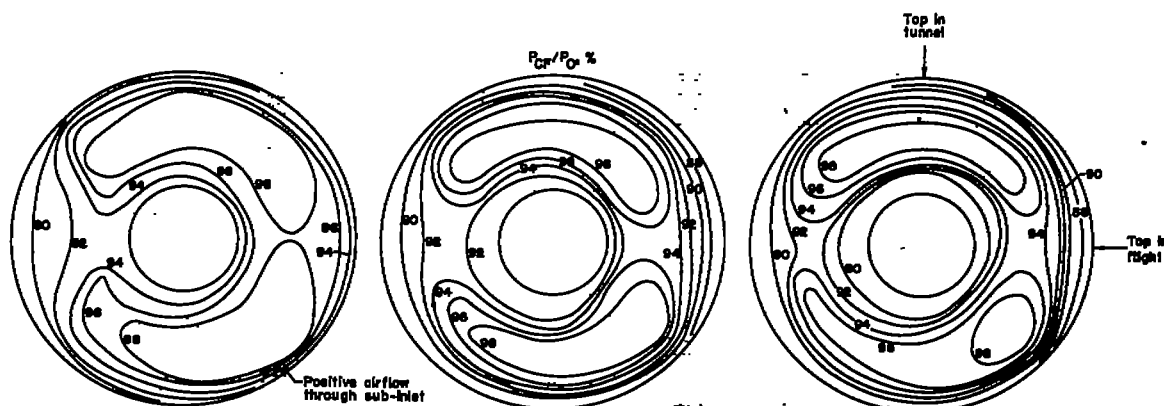


Figure 13. - Effect of angle of attack on total-pressure distortion and recovery at diffuser exit (compressor face) of supersonic nose inlet with constant corrected weight flow (engine mode of operation). Free-stream Mach number, 0.27.



Time in icing, min	0	3	6
Corrected weight flow, lb/sec	158.1	150.4	147.6
Total-pressure distortion, %	11.3	13.5	15.1
Total-pressure recovery	0.966	0.946	0.938
Inlet velocity ratio	1.58	1.45	1.41
Local static pressure			
Free-stream total pressure	0.835	0.832	0.829



C-39905

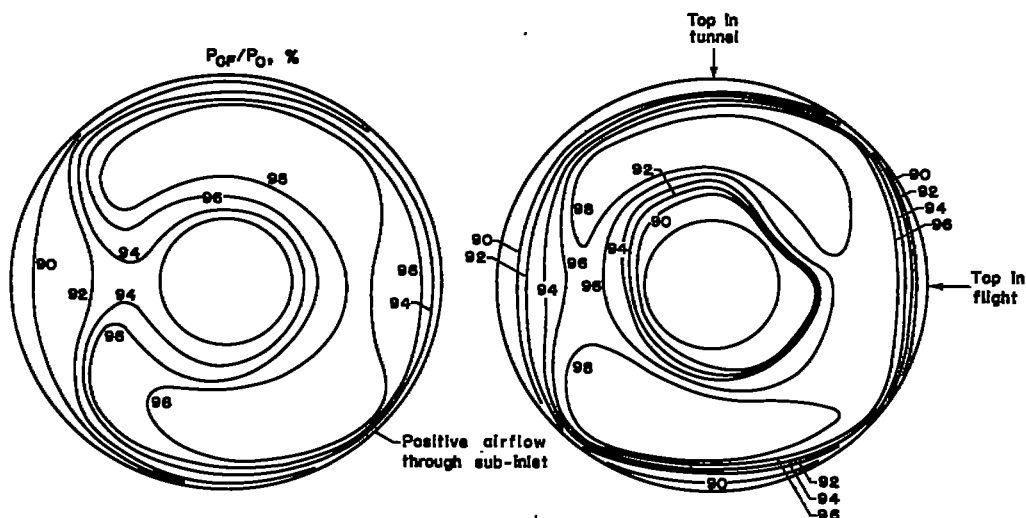


C-39985

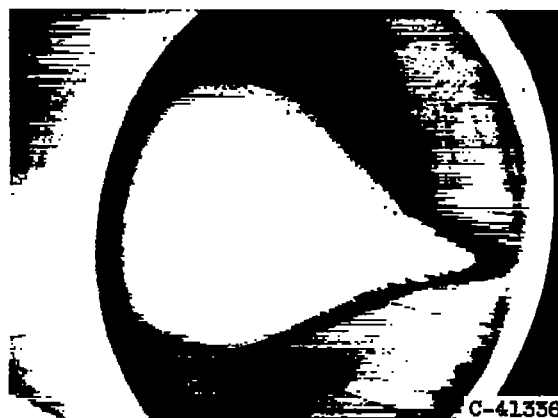
Photographs after 6 minutes of icing

(a) Run 9. Angle of attack,  $12^\circ$ ; free-stream Mach number, 0.27; free-stream static air temperature,  $15^\circ\text{F}$ ; liquid-water content, 1.3 grams per cubic meter; volume-median drop diameter, 16 microns.

Figure 14. - Maps of local to free-stream total-pressure ratio at compressor face and photographs of iced model.



Time in icing, min	0	$7\frac{1}{2}$
Corrected weight flow, lb/sec	160.0	156.8
Total-pressure distortion, %	11.5	12.1
Total-pressure recovery	0.965	0.953
Inlet velocity ratio	1.60	1.54
Local static pressure	0.830	0.825
Free-stream total pressure		

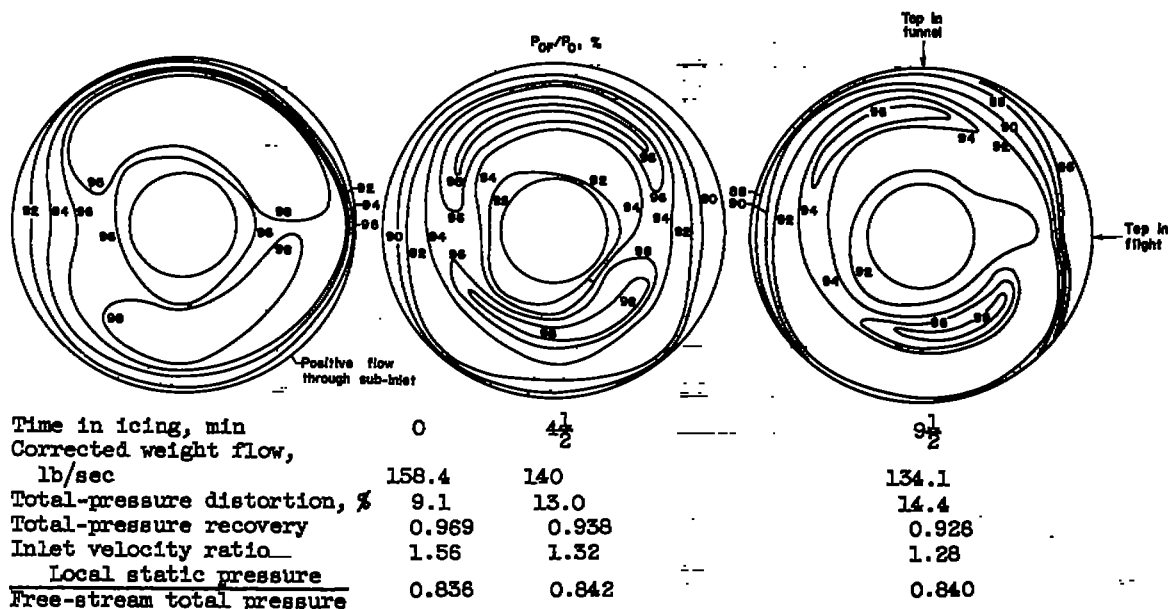


Photographs after  $10\frac{3}{4}$  minutes of icing

(b) Run 12. Angle of attack,  $12^\circ$ ; free-stream Mach number, 0.28; free-stream static air temperature,  $0^\circ\text{F}$ ; liquid-water content, 0.65 gram per cubic meter; volume-median drop diameter, 11 microns.

Figure 14. - Continued. Maps of local to free-stream total-pressure ratio at compressor face and photographs of iced model.





Ice formation before tunnel shutdown

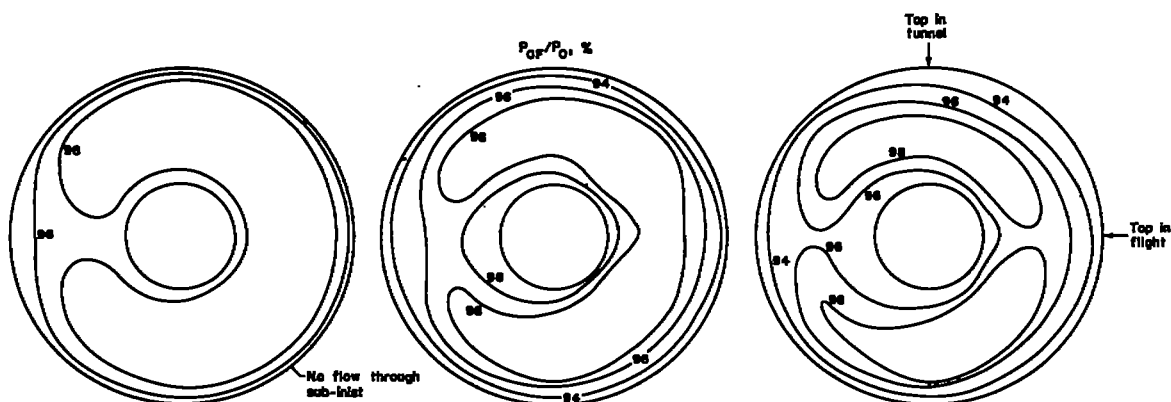


Ice formation after tunnel shutdown

Photographs after  $10\frac{1}{2}$  minutes of icing

(o) Run 13. Angle of attack,  $8^\circ$ ; free-stream Mach number, 0.27; free-stream static air temperature,  $15^\circ\text{F}$ ; liquid-water content, 1.3 grams per cubic meter; volume-median drop diameter, 16 microns.

Figure 14. - Continued. Maps of local to free-stream total-pressure ratio at compressor face and photographs of iced model.



Time in icing, min	0	2 $\frac{1}{4}$	5
Corrected weight flow, lb/sec	121.6	111.9	105.0
Total-pressure distortion, %	4.8	6.5	7.3
Total-pressure recovery	0.986	0.973	0.968
Inlet velocity ratio	1.19	1.09	1.04
Local static pressure	0.912	0.912	0.915
Free-stream total pressure			



Photographs after 5 minutes of icing

(d) Run 10. Angle of attack,  $12^\circ$ ; free-stream Mach number, 0.27; free-stream static air temperature,  $15^\circ$  F; liquid-water content, 1.3 grams per cubic meter; volume-median drop diameter, 16 microns.

Figure 14. - Concluded. Maps of local to free-stream total-pressure ratio at compressor face and photographs of iced model.